Encoderless Angle Estimation Methods for Rotary Electric Actuator

February 2018

Yuki SAITO

A Thesis for the Degree of Ph.D. in Engineering

Encoderless Angle Estimation Methods for Rotary Electric Actuator

February 2018

Graduate School of Science and Technology
Keio University

Yuki SAITO

Acknowledgements

I have completed this dissertation as a summary of my research from April 2010 through February 2013 and April 2015 through February 2018 as a member of Ohnishi Laboratory at Keio University. In particular, I decided to focus on research from 2015 to 2018 in this dissertation, as my master's thesis handles research completed by 2013. I would like to acknowledge those who have helped me to complete my research.

First of all, I would like to express my sincere gratitude to my supervisor, Professor Dr. Kouhei Ohnishi of Keio University. His enormous support and insightful comments were invaluable for my research. Activities in Ohnishi Laboratory were precious experiences for me.

I greatly appreciate the members of my Ph. D. dissertation committee, Professor Dr. Hiroaki Nishi, Associate Professor Dr. Takahiro Yakoh, and Associate Professor Dr. Ryogo Kubo of Keio University. Their comments and advices greatly helped to improve the thesis.

I gratefully acknowledge the members of SUM committee at Keio University, Professor Dr. Toshiyuki Murakami, Associate Professor Dr. Seiichiro Katsura, and Assistant Professor Dr. Takahiro Nozaki, for all their valuable advice and comments.

Dr. Shuhei Shimmyo of Keio University, Mr. Kazuki Tanida of Sumitomo Heavy Industries, Ltd., Dr. Koyo Yu of KEYENCE CORPORATION, Dr. Takuya Matsunaga of Kanagawa Institute of Industrial Science and Technology, Mr. Kasun Prasanga, and Mr. Kenji Ogawa provided a great deal of valuable and practical advice as the senior researchers in the laboratory. Without their guidance and persistent help, my Ph. D dissertation would not have been possible.

Furthermore, Mr. Hiromu Sekiguchi, Mr. Satoshi Fukushima, and Mr. Kazuma Nakai made enormous contributions to the projects and experiments, as well as making work in the laboratory very enjoyable. I received tremendous support with activities in Ohnishi Laboratory from Mr. Toshiaki Okano. Mr. Shuhei Akutsu and Mr. Takahiro Nakagawa of the Nozaki Laboratory helped my student life, and Mr. Xiaobai Sun, Mr. Yuta Tawaki, and Mr. Wanping Lyu of Ohnishi Laboratory helped with laboratory work. I would also like to thank all the students in Ohnishi and Nozaki laboratories.

I would like to offer my special thanks to Mr. Yusuke Ohshima, Mr. Wataru Iida, and Dr. Takahiro Mizoguchi of Motion Lib, Inc.; Dr. Akira Nagashima, Mr. Akiharu Machida, Mr. Hroshi Yazaki, Mr. Toshimitsu Uemura, and Mr. Katsumori Gyonouchi of the Haptics Research Center; and the employees of Yokogawa Electric Corporation. Their constructive comments and warm encouragement have been a great help in my research activities.

I am deeply grateful to my parents and sister for giving me tremendous support. Without their support, I could not have dedicated myself to this research.

There are many people who helped me although I could not mention all of them here. I would like to express my sincere gratitude again to the all the people who have supported me.

February, 2018
Yuki Saito

Contents

List of Figures

List of Tables

Chapter 1

Introduction

1.1 Background

In recent years, there has been an increase in the demand for electric actuators. Heretofore, electric actuators were mainly used in the industrial field. However, recently, they are being incorporated into many consumer electronic devices. Furthermore, the applications of medical robots and nursing robots have also expanded. Moreover, recent researches have promoted the development of human assist robots[1–7]. With the increase in demand for such applications, there has been an increase in the demand for small electric actuators.

Electric actuators can be roughly classified into direct current (DC) motors and alternate current (AC) motors, as shown in Fig. 1-1. In addition, AC motors can be classified into induction motors, permanent magnet synchronous motors (PMSM), and reluctance motors. For applications related to robots, a highly accurate control is required, especially in the low-speed region. Therefore, brushed DC (BDC) motors and brushless DC (BLDC) motors, which have high control performance in the low-speed region, are widely used. The BLDC motor is categorized as a PMSM. Furthermore, the control is achieved by using high-resolution mechanical sensors such as encoders. However, a mechanical sensor has drawbacks such as increase in the size of the entire system, increase in the cost of the robot, increase in the number of connections, increase in the failure rate, and increase in the maintenance cost. These disadvantages are obstacles to the advancement of both the electric actuator industry and the robot industry. Therefore, techniques to estimate the angle and velocity of the rotor without any mechanical sensors are proposed[8–13].

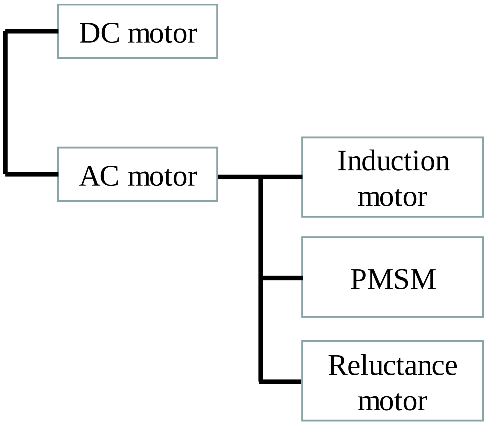

Fig. 1-1: Types of electric actuators.

1.2 Previous researches and orientation of this research

Encoderless estimation methods for the PMSM have been studied extensively. Estimation methods can be roughly classified into methods based on the counter electromotive force (EMF) [14–18], methods based on the saliency of the motor [19–24], and methods using low-resolution sensors such as Hall sensor [25–28]. However, in the research field of encoderless estimation, the improvement of estimation accuracy in industrial applications is the mainstream. Therefore, the estimation accuracy around the zero-speed region is not considered. In the estimation method based on the counter EMF, the desired signal around the zero-speed region is hidden by noise and cannot be detected. Thus, accurate estimation of the angular velocity is impossible. In the technique based on the saliency of the motor, the angle is estimated by measuring the inductance with angle dependency. However, most methods focus on the frequency of the inductance. Therefore, they cannot perform accurate estimation around the zero-speed region. Similarly, even in methods using low-resolution sensors, complementary methods for estimating the angle in the high-speed region have been proposed.

Although not as much as that for the PMSM, many encoderless estimation methods have been proposed for the BDC motor. Kambara et al. proposed counter EMF observer (CFOB) for the BDC motor and estimated the angular velocity by using the estimation result from the observer [29, 30]. However, as mentioned before, methods using the counter EMF cannot perform accurate estimation around the zero-speed region. Radcliffe et al. focused on inductive spikes and estimated the angular velocity by observing their periods [31]. Estimation methods based on the frequency of the current ripple have also been proposed [32–34]. These methods focus on estimation in the high-speed region. Knezevic et al. aimed to perform angle estimation in the low-speed region, and proposed a direct angle-estimation method using the shape of the current ripple [35]. However, the estimation error increases around the zero-speed region.

1.3 Chapter organization

The rest of this thesis is organized as shown in Fig. 1-2. This paper aims to realize highly accurate encoderless angle estimation around the zero-speed region. The purpose of this paper is twofold: first, to achieve high accuracy angle estimation of the BLDC motor by using only a Hall sensor; second, to realize high accuracy angle estimation of the BDC motor by using only electrical signals.

Chapter 2 describes the motion control based on robust acceleration control. As a method to realize robust control, Disturbance OBserver (DOB) is explained. Then, Reaction Torque OBserver (RTOB), which estimates the environmental reaction torque is explained. The angle control and torque control based on the acceleration control are introduced. Furthermore, as a space restricted application, the motion control of a two-link manipulator equipped with a biarticular muscle mechanism, which is considered to be utilized for humanoids, is outlined.

Chapter 3 presents an algorithm to achieve precise angle estimation by using digital Hall signals and counter EMF for a BLDC motor. This method uses Hall sensors for accurate and periodic detection of the position. In addition, interpolation between the detection positions is performed using the counter EMF. By using the proposed method, accurate smooth position information can be obtained, and a high-performance operation can be achieved. The effectiveness of the proposed approach is verified through simulations and experiments.

Chapter 4 describes the sensorless angle estimation method for the BDC motor. In order to estimate the angle of the rotor without any mechanical sensors, the proposed method uses impedance variation by contact switching. The impedance is measured by using high-frequency signal injection and discrete Fourier transform. This method can be used to estimate the angle of the rotor directly. Therefore, it is possible to estimate the angle accurately at low speeds. The validity of the proposed method is verified through experiments.

Chapter 5 concludes this research. The symbols and subscripts are shown as in Table 1.1 and Table 1.2.

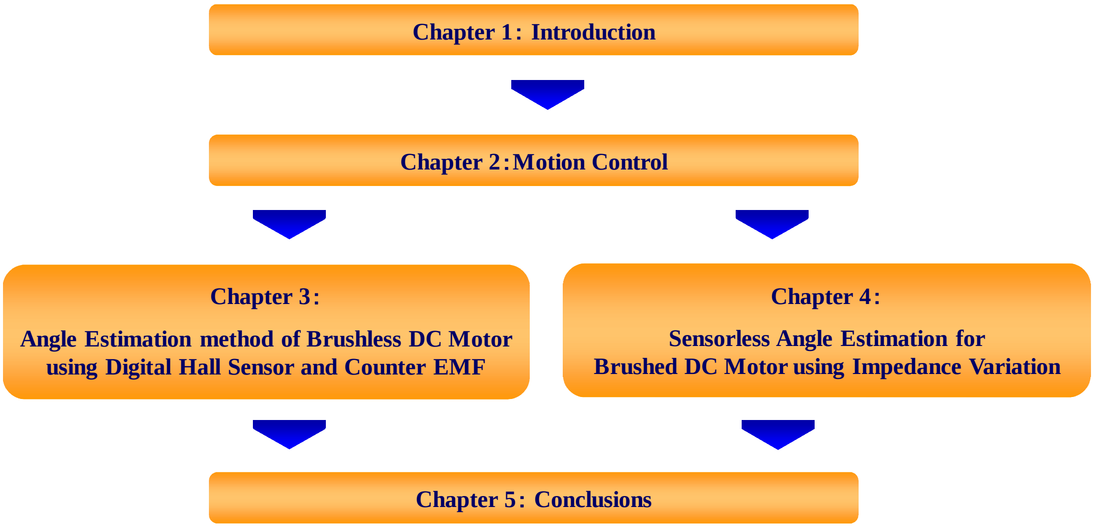

Fig. 1-2: Chapter organization.

Table 1.1: Symbols utilized in this thesis

Symbols	Descripsions	Units
θ, Θ	Angle	rad
τ, T	Torque	Nm
J	Moment of Inertia	$\mathrm{kg}\cdot\ \mathrm{m}^2$
K_t	Torque constant	Nm/A
i, I	Current	A
v, V	Voltage	V
R	Resistance	Ω
L	Inductance	H
Z	Impedance	Ω
M	Mutual inductance	H
ω	Angular velocity	rad/s
e	counter EMF	V
Ψ	Armature flux linkage	Wb
Φ	Interlinkage magnetic flux	Wb
s	Laplace operator	-
p	Differential operator	-
g	Cutoff frequency	rad/s

Table 1.2: Superscripts and subscripts utilized in this thesis

Superscripts and subscripts	Descripsions
$\bigcirc_{m}$	Motor
$\bigcirc_{a}$	Armature
$\bigcirc_{load}$	Load
$\bigcirc_{dis}$	Disturbance
$\bigcirc_{int}$	Internal
$\bigcirc_{ext}$	External
$\bigcirc_{c}$	Coulomb friction
$\bigcirc_{g}$	Gravity
$\bigcirc_{fluct}$	Fluctuation
$\bigcirc_{env}$	Environmental
$\bigcirc_{u,v,w}$	Phase of u, v, w
$\bigcirc_{\alpha,\beta}$	Axes of α, β
$\bigcirc_{d,q}$	Axes of d, q
$\bigcirc_{L}$	Low frequency band
$\bigcirc_{H}$	High frequency band
$\bigcirc^{cmd}$	Command
$\bigcirc^{ref}$	Reference
$\bigcirc^{res}$	Response
$\dot{\bigcirc}$	First order differential
$\ddot{\bigcirc}$	Second order differential
$\hat{\bigcirc}$	Estimated value

Chapter 2

Motion control and biological mechanism

2.1 Introduction

This chapter describes motion control based on robust acceleration control and a two-link manipulator equipped with a biarticular muscle mechanism. First, a simple model of rotary motors and their dynamics are explained in Section 2.2. Second, as a method to realize the robust control, disturbance observer (DOB) is explained. Next, reaction torque observer (RTOB), which estimates the environmental reaction torque is explained. The angle and torque controls based on acceleration control are introduced in Section 2.5. Furthermore, as a space-restricted application, the motion control of a two-link manipulator equipped with a biarticular muscle mechanism considered for use in humanoid machines is outlined.

2.2 Modeling of rotary motor

This section describes a simple rotary motor model. The driving torque of the rotary motor τ_m is given by

$$\tau_m = K_t i_a, \tag{2.1}$$

where, K_t is the torque constant and i_a is the armature current of the rotary motor. The motion equation of the rotary motor is given by (2.2) using the moment of inertia of the rotary motor J_m, and the angle response θ^{res}.

$$\tau_m = J_m \ddot{\theta}^{res} \tag{2.2}$$

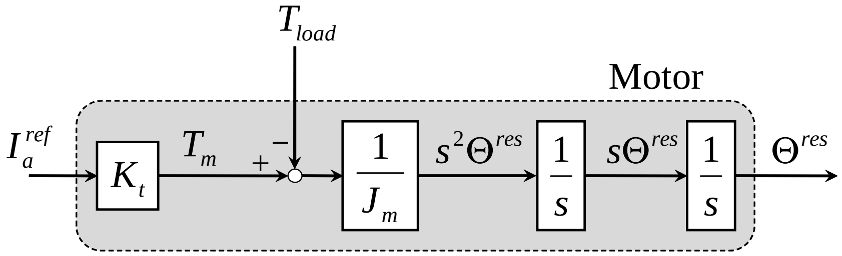

Fig. 2-1: Dynamics of rotary motor.

When the gain of the inner-loop current controller is sufficiently large, the current reference i_a^{ref} and armature current of the rotary motor i_a can be regarded as the same value. Therefore, (2.3) is derived.

$$\tau_m = J_m\ddot{\theta}^{res} = K_t i_a^{ref} \tag{2.3}$$

In a practical driving system, the external torque due to contact with the environment and the load torque due to gravity and friction can be observed. Assuming that the full load torque applied to the motor is τ_{load}, the dynamics of the rotary motor is expressed by (2.4).

$$J_m\ddot{\theta}^{res} = K_t i_a^{ref} - \tau_{load} \tag{2.4}$$

Furthermore, (2.4) is rewritten as (2.5) by Laplace transformation.

$$J_m s^2\Theta^{res} = K_t I_a^{ref} - T_{load} \tag{2.5}$$

Here, Θ, I, T, and s are the frequency-domain representations of θ, i, τ, and the Laplace operator, respectively. The block diagram is shown in Fig. 2-1. The load torque T_{load} is represented by

$$T_{load} = T_{ext} + T_{int} + T_g + T_c + Ds\Theta^{res}, \tag{2.6}$$

where T_{ext}, T_{int}, T_g, T_c, and $Ds\Theta^{res}$ denote the external torque affecting the system, internal interference torque such as Coriolis or centrifugal torque, torque generated by gravitational acceleration, Coulomb friction, and viscous-frictional torque, respectively.

In an actual system, the inertia J_m and torque constant K_t vary from the nominal values J_{mn} and K_{tn}

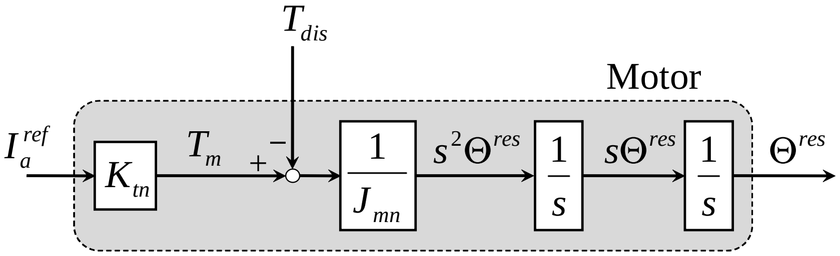

Fig. 2-2: Dynamics of rotary motor based on nominal model.

as follows.

$$\begin{aligned} J_m &= J_{mn} + \Delta J_m && (2.7) \\ K_t &= K_{tn} + \Delta K_t && (2.8) \end{aligned}$$

The fluctuation torque T_{fluct} caused by the above parameter variations is expressed by

$$T_{fluct} = \Delta J_m s^2 \Theta^{res} - \Delta K_t I_a^{ref}. \tag{2.9}$$

Hence, the disturbance T_{dis} including the load torque T_{load} and parameter variations is derived as

$$\begin{aligned} T_{dis} &= T_{load} + T_{fluct}, \\ &= T_{ext} + T_{int} + T_g + T_c + Ds\Theta^{res} + \Delta J_m s^2 \Theta^{res} - \Delta K_t I_a^{ref}. && (2.10) \end{aligned}$$

Thus, the dynamics of the rotary motor based on the nominal model is expressed by (2.11) and Fig. 2-2.

$$J_{mn} s^2 \Theta^{res} = K_{tn} I_a^{ref} - T_{dis} \tag{2.11}$$

2.3 Disturbance observer

The typical outputs in motion control are angle and torque. The second differential of the angle is acceleration, which is calculated by dividing torque by inertia. Thus, acceleration is a common factor between the angle and the torque. Therefore, if the acceleration can be controlled with high accuracy, then the angle and the torque can be controlled with high accuracy as well. For this reason, this section

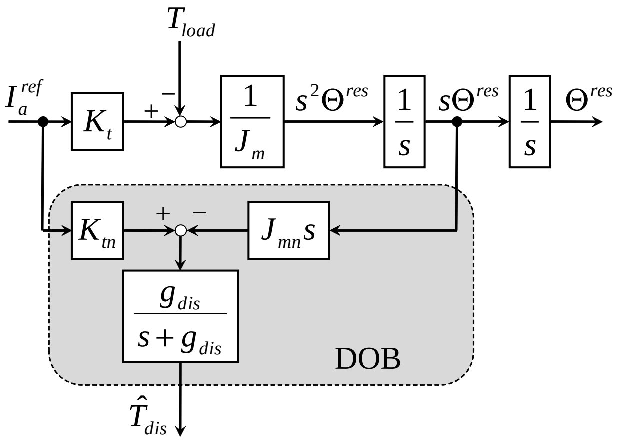

Fig. 2-3: Disturbance observer.

describes acceleration-based robust motion control. By using the deformation in (2.11), the disturbance T_{dis} is expressed by

$$T_{dis} = K_{tn}I_a^{ref} - J_{mn}s^2\Theta^{res}. \tag{2.12}$$

Disturbance observer (DOB) estimates the disturbance torque T_{dis} from the input and output of the motor. DOB achieves robust motion control via the compensation current I_{cmp} obtained from the estimated disturbance $\hat{T}_{dis}$ [36]. The disturbance torque T_{dis} is estimated by the current reference I_a^{ref} and acceleration response $s^2\Theta^{res}$. The acceleration response is calculated by the second differential of the angle response or the first differential of the angular velocity response. However, when differentiation is performed in the control system, the influence of high-frequency noise caused by the quantization error of the encoder included in the disturbance becomes large. Therefore, by incorporating a pseudo-derivative including a low-pass filter (LPF), the influence of the high-frequency noise can be suppressed, and the estimated disturbance is obtained as

$$\hat{T}_{dis} = \frac{g_{dis}}{s + g_{dis}}T_{dis}. \tag{2.13}$$

Here, g_{dis} is the cutoff frequency of DOB. The block diagram of DOB is shown in Fig. 2-3, and is expressed by the integrator and feedback of the compensation current, as shown in Fig. 2-4. The feedback from the compensation current provides the robust acceleration control.

Fig. 2-4 can be equivalently converted to Fig. 2-5. the low-frequency band of the disturbance T_{dis} is suppressed by a high-pass filter (HPF). The HPF $G_s(s)$ is called the sensitivity function, which means

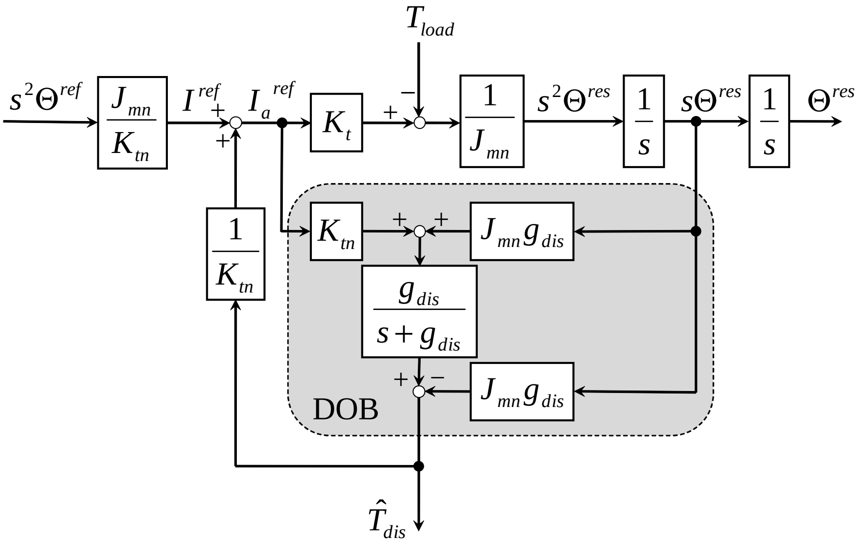

Fig. 2-4: Feedback of estimated disturbance using disturbance observer.

that the disturbance does not affect the low-frequency band with frequencies of less than g_{dis}, though it will impact the high-frequency band, at frequencies greater than g_{dis}.

$$G_s(s) = \frac{s}{s + g_{dis}} \tag{2.14}$$

Assuming that the error between the input acceleration reference and the actual acceleration is p, the control system becomes Fig. 2-6. The equivalent acceleration disturbance p is the error of the control system in the acceleration dimension. The amplitude of the equivalent acceleration disturbance p is determined by the performance of the sensitivity function $G_s(s)$.

$$\begin{aligned} p &\equiv s^2\Theta^{ref} - s^2\Theta^{res} \\ &= {J_{mn}}^{-1}G_s(s)T_{dis} \end{aligned} \tag{2.15}$$

2.4 Reaction torque observer

Reaction torque observer (RTOB) [37,38] is the application of DOB. DOB estimates and compensates all disturbances, whereas RTOB is an observer that estimates only the environmental reaction torque

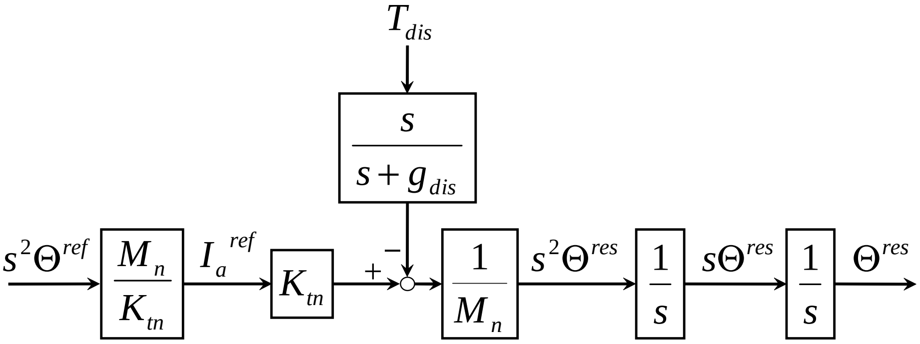

Fig. 2-5: Equivalent block diagram of robot system.

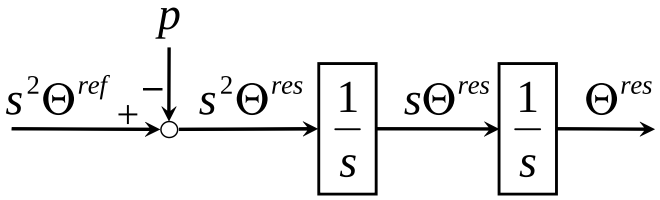

Fig. 2-6: Equivalent acceleration disturbance.

T_{env}, which is almost equivalent to the external torque T_{ext}. The block diagram of RTOB is shown in Fig. 2-7. In the rotary motor, the load torque, excluding the viscous-friction, can be neglected. Furthermore, assuming that the nominal torque constant K_{tn} matches the actual torque constant K_t, the environmental reaction torque T_{env} is derived as

$$T_{env} = T_{dis} - Ds\Theta^{res} - \Delta J_m s^2\Theta^{res}. \tag{2.16}$$

Equation (2.16) denotes that the environmental reaction torque can be obtained by subtracting the viscous-frictional torque and the influence of inertial variation from the disturbance torque. Thus, the estimated environmental reaction torque is given by

$$\hat{T}_{env} = \frac{g_{reac}}{s+g_{reac}} T_{env}. \tag{2.17}$$

the inertial variation ΔJ_m can be identified by a constant-acceleration test, and the viscous-frictional coefficient D can be identified by a constant-velocity test.

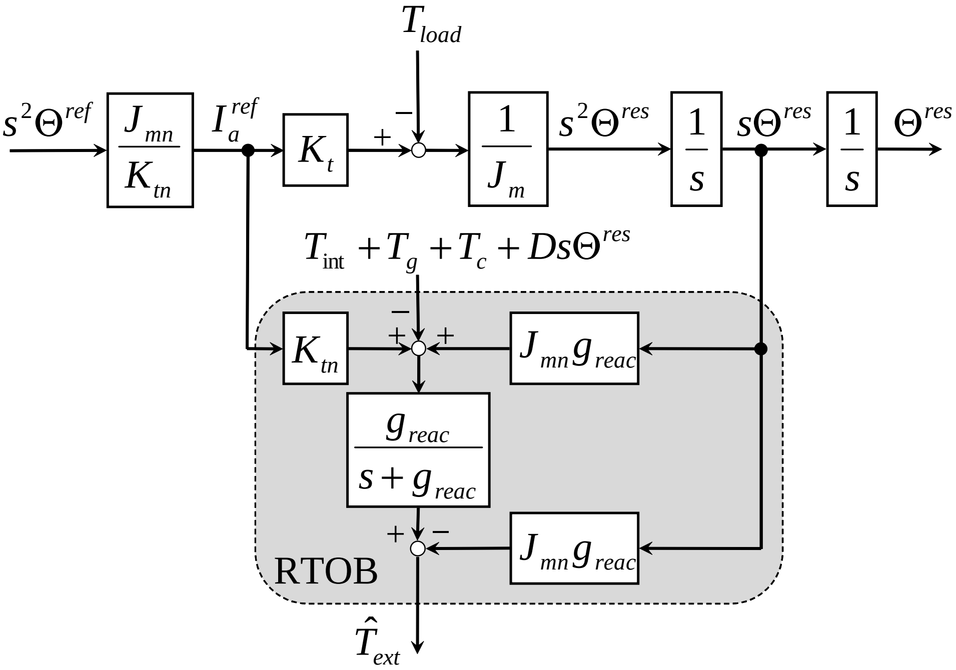

Fig. 2-7: Reaction torque observer.

2.4.1 Constant-velocity test

By moving the motor at a constant speed without touching the environment, the viscous-friction torque can be extracted from (2.16) and derived as

$$T_{dis} = Ds\Theta^{res}. \tag{2.18}$$

Because the viscous-friction torque is linear, DOB can estimate the viscous-friction coefficient from the output.

2.4.2 Constant-acceleration test

By removing the viscous-frictional torque obtained by the constant-velocity test from the output of DOB and providing a constant acceleration input, the disturbance due to inertial variation is extracted as

$$\hat{T}_{dis} - \hat{D}s\Theta^{res} = (J_m - J_{mn})\, s^2\Theta^{res} = \Delta J_m s^2\Theta^{res}. \tag{2.19}$$

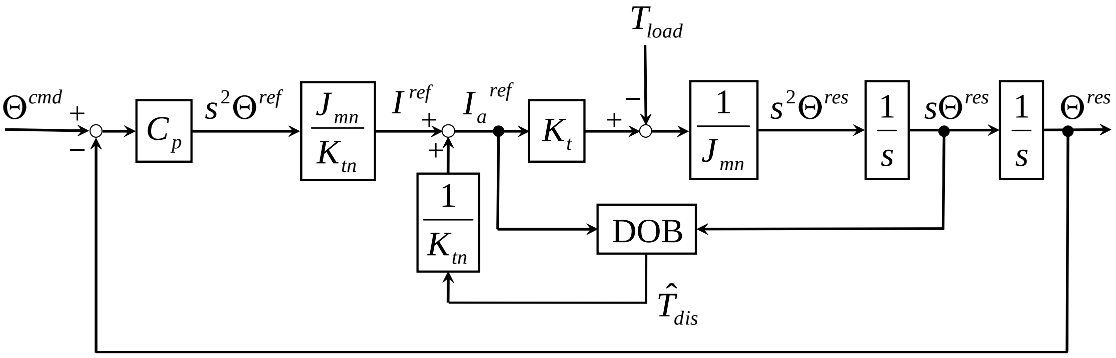

Fig. 2-8: Angle control using disturbance observer.

Therefore ΔJ_m can be identified by

$$\Delta J_m = \frac{1}{s^2\Theta^{res}}\left(\hat{T}_{dis} - \hat{D}s\Theta^{res}\right). \tag{2.20}$$

2.5 Acceleration-based control system

Acceleration is a low-order state variable in the dynamical system, and if the acceleration can be controlled, the angle and the torque can be controlled with high accuracy. This section describes the angle control and torque control and, derives the acceleration reference from the angle and torque controllers.

2.5.1 Angle control

In order to perform ideal angle control, regardless of any disturbance or parameter variations, the angle output must follow the desired value. This is equivalent to the fact that the transfer function from the angle command to the angle response becomes 1, as

$$\frac{\Theta^{res}}{\Theta^{cmd}} = 1. \tag{2.21}$$

Assuming the system is a second-order system, the acceleration reference $s^2\Theta^{ref}$ is expressed by (2.22) using the proportional gain K_p and derivative gain K_v.

$$s^2\Theta^{ref} = s^2\Theta^{cmd} + K_v\left(s\Theta^{cmd} - s\Theta^{res}\right) + K_p\left(\Theta^{cmd} - \Theta^{res}\right) \tag{2.22}$$

In general angle PD control systems, the acceleration reference is calculated by removing the first term on the right side of (2.22). In a nominal model system that does not take into consideration the effects of disturbance and parameter variations, the response becomes critical damping when (2.23) is satisfied. The convergence is fast, and the response with no vibration can be obtained.

$$K_v = 2\sqrt{K_p} \tag{2.23}$$

Thus, (2.22) can be written as follows by using PD controller $C_p(s)$.

$$C_p\left(s\right) = K_p + K_v s \tag{2.24}$$

$$s^2 X^{ref} = C_p\left(s\right)\left(X^{cmd} - X^{res}\right) \tag{2.25}$$

The block diagram of angle control using DOB is shown in Fig. 2-8.

2.5.2 Torque control

The ideal torque control tracks the actual force output to the desired value. Therefore, the acceleration reference $s^2\Theta^{ref}$ can be determined by calculating the error between the torque command and the environmental reaction torque as the torque response, such as in

$$s^2\Theta^{ref} = C_f\left(s\right)\left(T^{cmd} - T_{env}\right), \tag{2.26}$$

$$C_f\left(s\right) = K_f. \tag{2.27}$$

In the equation, $C_f(s)$ is the torque controller, which is assumed to be equal to the torque gain K_f in this paper. When DOB is used in torque control, the relationship between the torque command and the environmental reaction torque is as follows.

$$T^{cmd} - T_{env} = \frac{1}{K_f}s^2\Theta^{res} - \frac{1}{K_f}\cdot\frac{s}{s+g_{dis}}T_{dis} \tag{2.28}$$

From (2.28), the error between the torque command and the environmental reaction torque is reduced as the torque gain increases. The block diagram of torque control using DOB and RTOB is shown in Fig. 2-9.

2.6 Two-link manipulator equipped with biarticular muscle mechanism

The technology for realizing humanoid robots is in development. In order to accomplish such machines, the incorporation of a biological mechanism is indispensable [39–42]. As an example of motion control, this section introduces a two-link manipulator equipped with a biarticular muscle mechanism.

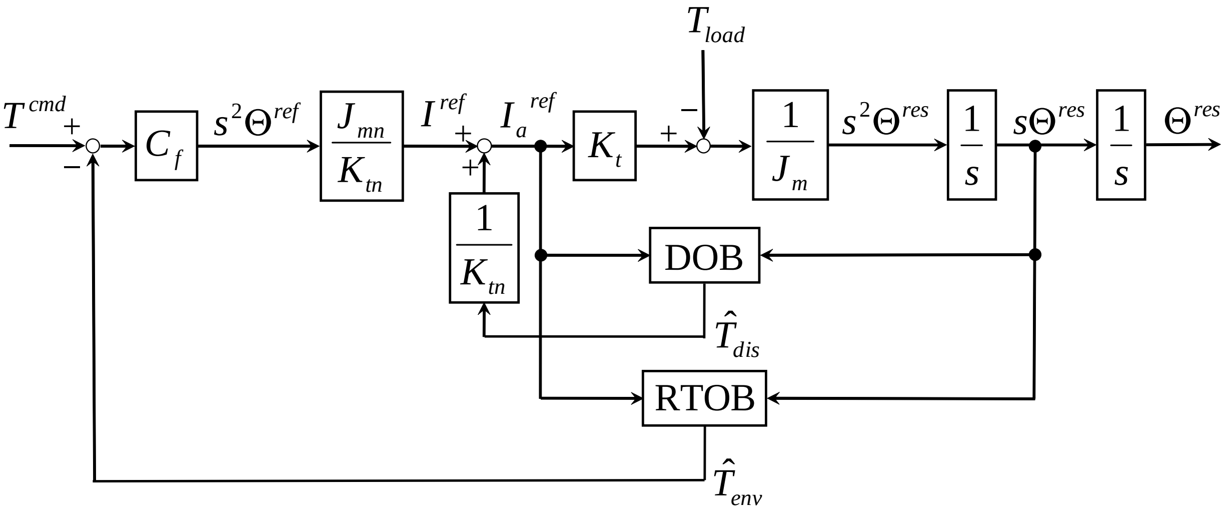

Fig. 2-9: Torque control using disturbance obserber and reaction torque observer.

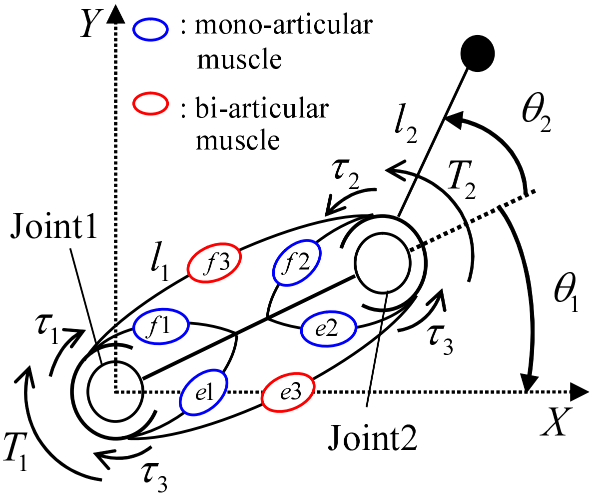

Fig. 2-10: Two-link manipulator with muscle model.

2.6.1 Modeling

A model of three pairs of antagonistic muscle mechanisms is shown in Fig. 2-10, where $f1$, $e1$, $f2$, and $e2$ represent monoarticular muscles, and $f3$ and $e3$ represent biarticular muscles. The kinematics of the two-link manipulator is expressed by

$$x = l_1 \cos\theta_1 + l_2 \cos(\theta_1 - \theta_2), \tag{2.29}$$

$$y = -l_1 \sin\theta_1 - l_2 \sin(\theta_1 - \theta_2), \tag{2.30}$$

where l_1 and l_2 are the length of each link. From these equations, the Jacobian matrix $\mathbf{J}_{\boldsymbol{aco}}$ is derived as (2.31)

$$\left.\begin{array}{rcl} \mathbf{J}_{\boldsymbol{aco}} & = & \begin{pmatrix} J_{aco11} & J_{aco12} \\ J_{aco21} & J_{aco22} \end{pmatrix} \\ J_{aco11} & = & -l_1 \sin\theta_1 - l_2 \sin(\theta_1 - \theta_2) \\ J_{aco12} & = & l_2 \sin(\theta_1 - \theta_2) \\ J_{aco21} & = & -l_1 \cos\theta_1 - l_2 \cos(\theta_1 - \theta_2) \\ J_{aco22} & = & l_2 \cos(\theta_1 - \theta_2) \end{array}\right\} \tag{2.31}$$

The Jacobian matrix can transform the joint space to a workspace as

$$\dot{\mathbf{x}} = \mathbf{J}_{\boldsymbol{aco}} \dot{\boldsymbol{\theta}}. \tag{2.32}$$

Here,

$$\mathbf{x} = [x\ y]^T, \tag{2.33}$$

$$\boldsymbol{\theta} = [\theta_1\ \theta_2]^T. \tag{2.34}$$

The two-link manipulator of this section is the plane configuration. Therefore, the effect of gravity can be ignored. Furthermore, the centripetal and Coriolis forces are exceedingly small. Thus, the dynamics is expressed by

$$\mathbf{T} = \mathbf{M}_n \ddot{\boldsymbol{\theta}}, \tag{2.35}$$

where

$$\mathbf{T} = [T_1\ T_2]^T, \tag{2.36}$$

$$\left.\begin{array}{rcl} \mathbf{M}_n & = & \begin{pmatrix} M_{11} & 0 \\ 0 & M_{22} \end{pmatrix} \\ M_{11} & = & m_1 l_{g1}^2 + m_2 l_1^2 + m_2 l_{g2}^2 + J_1 + J_2 + 2 m_2 l_1 l_{g2} \cos\theta_2 \\ M_{22} & = & m_2 l_{g2}^2 + J_2 \end{array}\right\}. \tag{2.37}$$

In the above equations, $\mathbf{M}_n$, $J_\circ$, $m_\circ$, and $l_{g\circ}$ are the nominal mass matrix, inertia moment of each joint, mass of each link, and distance to the center of each link, respectively. In this paper, the output of each muscle is defined as $F_*, (* = f1, e1, f2, e2, f3, e3)$. The torque of each joint is expressed by

$$\begin{aligned} T_1 &= \tau_1 + \tau_3, && (2.38)\\ T_2 &= \tau_2 + \tau_3. && (2.39) \end{aligned}$$

Here,

$$\begin{aligned} \tau_1 &= r(F_{f1} - F_{e1}), && (2.40)\\ \tau_2 &= r(F_{f2} - F_{e2}), && (2.41)\\ \tau_3 &= r(F_{f3} - F_{e3}). && (2.42) \end{aligned}$$

Equations (2.38) and (2.39) can be written as follows.

$$\begin{aligned} \mathbf{T} &= \mathbf{G}\boldsymbol{\tau} && (2.43)\\ \mathbf{G} &= \begin{pmatrix} d_1 & 0 & d_3 \\ 0 & d_2 & d_3 \end{pmatrix} && (2.44)\\ \boldsymbol{\tau} &= \begin{pmatrix} \frac{\tau_1}{d_1} & \frac{\tau_2}{d_2} & \frac{\tau_3}{d_3} \end{pmatrix}^T && (2.45) \end{aligned}$$

Here, d_1, d_2, and d_3 are the desired real numbers. This section refers to $\mathbf{G}$ as a moment arm matrix. The problem of torque sharing is solved by utilizing a pseudo inverse-moment arm matrix $\mathbf{G}^+$, represented by

$$\begin{aligned} \mathbf{G}^+ &= \mathbf{G}^T\left(\mathbf{G}\mathbf{G}^T\right)^{-1} \\ &= \frac{1}{D}\begin{pmatrix} d_1 d_2^2 + d_1 d_3^2 & -d_1 d_3^2 \\ -d_2 d_3^2 & d_1^2 d_2 + d_2 d_3^2 \\ d_2^2 d_3 & d_1^2 d_3 \end{pmatrix}, && (2.46)\\ D &= d_1^2 d_2^2 + d_2^2 d_3^2 + d_3^2 d_1^2, && (2.47)\\ \boldsymbol{\tau} &= \mathbf{G}^+\mathbf{T}, && (2.48) \end{aligned}$$

2.6.2 Mechanism and control system

A proposed mechanical model of the two-link manipulator is shown in Fig. 2-11. The biarticular muscle mechanism is composed of four linear motors. The monoarticular muscle mechanism is composed

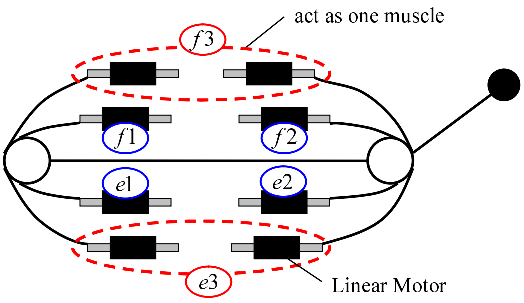

Fig. 2-11: Model of two-link manipulator.

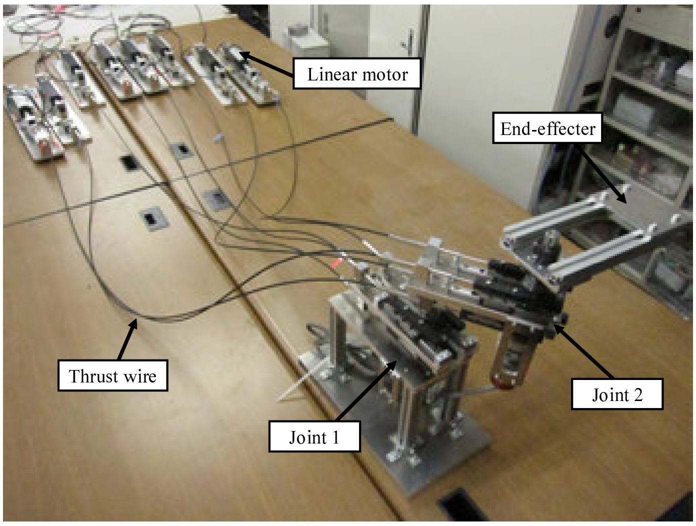

Fig. 2-12: Two-link manipulator (entire picture).

of two linear motors. Therefore, the two-link manipulator is actuated by eight linear motors. The overall view of the two-link manipulator is shown in Fig. 2-12.

In this section, an antagonistic control system is proposed. Furthermore, a biarticular muscle control sysmtem combining the antagonistic control system and the moment arm matrix is proposed. A block diagram of the proposed system is shown in Fig. 2-13, in which the broken line represents the antagonistic control system. The details are shown in Fig 2-14. The transformation matrix $\mathbf{H}$ in Fig. 2-14 is expressed as

$$\mathbf{H} = \begin{pmatrix} 1 & 1 \\ 1 & -1 \end{pmatrix}. \tag{2.49}$$

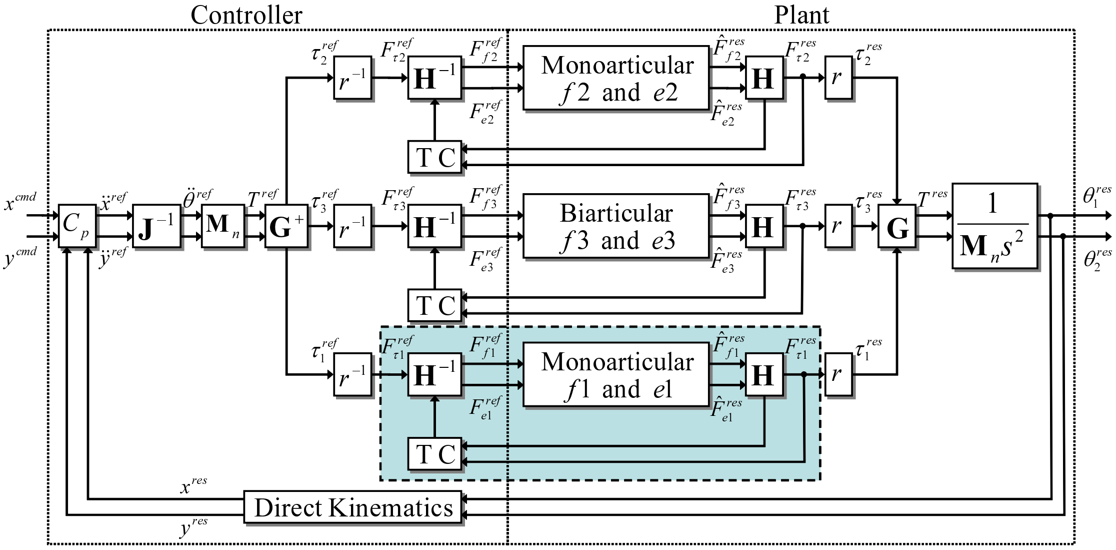

Fig. 2-13: Block diagram of biarticular control system.

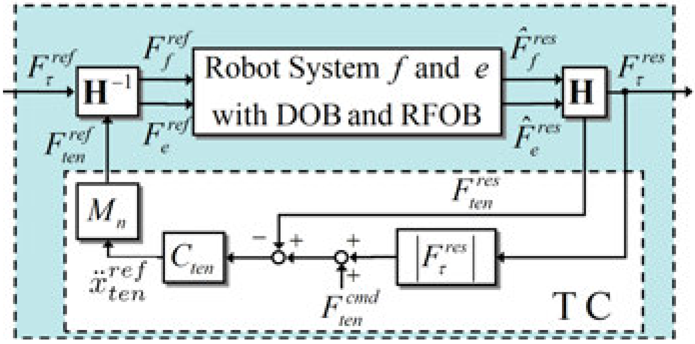

Fig. 2-14: Block diagram of antagonistic control system.

The relation between the tension response F_{ten}^{res}, the antagonistic muscle output response F_τ^{res}, and each muscle output response $\hat{F}_f^{res}$, $\hat{F}_e^{res}$ is expressed by (2.50).

$$\begin{pmatrix} F_{ten}^{res} \\ F_\tau^{res} \end{pmatrix} = \mathbf{H} \begin{pmatrix} \hat{F}_f^{res} \\ \hat{F}_e^{res} \end{pmatrix} \tag{2.50}$$

When the minimum value of the tension is set by F_{ten}^{cmd}, the acceleration reference in antagonism control is derived as

$$\ddot{x}_{ten}^{ref} = C_{ten} \left(|F_\tau^{res}| + F_{ten}^{cmd} - F_{ten}^{res} \right). \tag{2.51}$$

Furthermore, the acceleration reference in position control is expressed as

$$\ddot{\mathbf{x}}^{ref} = C_p \left(\mathbf{x}^{cmd} - \mathbf{x}^{res} \right). \tag{2.52}$$

In (2.51) and (2.52), C_{ten} and C_p are the proportional force controller and the proportional-derivative position controller, expressed as

$$\begin{aligned} C_{ten} &= K_{ten}, & (2.53) \\ C_p &= K_p + K_v s. & (2.54) \end{aligned}$$

The antagonist muscle output reference F_{τ}^{ref} and the tension reference F_{ten}^{ref} are obtained from the muscle output reference using the inverse matrix $\mathbf{H}^{-1}$, as in

$$\begin{pmatrix} F_f^{ref} \\ F_e^{ref} \end{pmatrix} = \mathbf{H}^{-1} \begin{pmatrix} F_{ten}^{ref} \\ F_{\tau}^{ref} \end{pmatrix}. \tag{2.55}$$

Thus, the force references of each linear motor are calculated.

2.6.3 Experiment

Outline of experiment

At the position command in this experiment, in order to avoid the singularity point where the determinant of the Jacobian matrix becomes zero, the command to bend the second joint by 90° is given in 10 seconds. After that, the command was set to (2.56) and (2.57).

$$\begin{aligned} x_{cmd} &= 0.115 + 0.03 \sin \left(\frac{2}{15} \pi t \right) & (2.56) \\ y_{cmd} &= 0.205 - 0.03 \cos \left(\frac{2}{15} \pi t \right) & (2.57) \end{aligned}$$

These equations indicate that the command was a circular orbit with a radius of 3 cm in 15 seconds. Here, the tension command was set to 1 N. The values of $d1$, $d2$, and $d3$ in the moment arm matrix were set to 1.0. The parameters utilized in this study are shown in Table 2.1

Experimental results

The experimental result of position control is shown in Fig. 2-15 and 2-16. From Fig. 2-15, although a minor error occurred due to the influence of static friction, accurate position tracking was achieved using

Table 2.1: Parameters utilized in experiment.

Symbol	Meanings of the parameter	Value
K_p	Position feedback gain	1600 $1/s^2$
K_v	Velocity feedback gain	500 $1/s$
K_{ten}	Force feedback gain	0.8
g_{dis}	Cutoff frequency of DOB	50 rad/s
g_{reac}	Cutoff frequency of RFOB	50 rad/s
M_n	Nominal mass	0.5 kg
K_{tn}	Nominal thrust constant	1.0 N/A
l_1	Length of link1	0.115 m
l_2	Length of link2	0.175 m
l_{g1}	Length to center of gravity of link1	0.0652 m
l_{g2}	Length to center of gravity of link2	0.0307 m
m_1	Mass of link1	1.474 kg
m_2	Mass of link2	0.865 kg
r	Radius of rotation of joint	0.015 m

the proposed control system. Furthermore, from Fig. 2-16, the realization of an antagonistic drive by the proposed antagonistic control system was confirmed. In addition, the distribution of the muscle outputs was demonstrated by the proposed biarticular control system using the moment arm matrix.

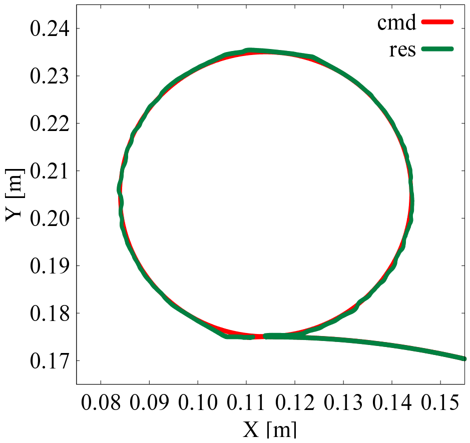

(a) Position response of circular orbit.

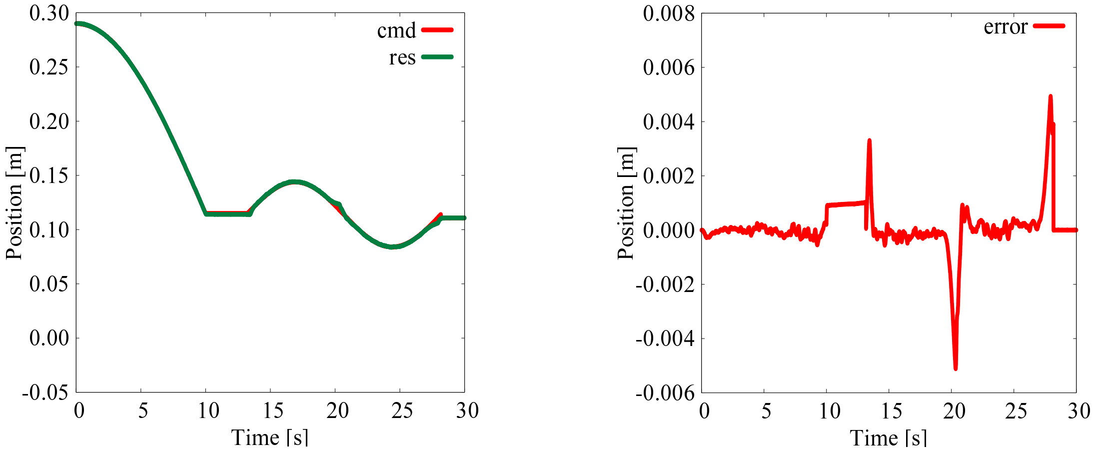

(b) Position response of x axis.

(c) Error in x axis.

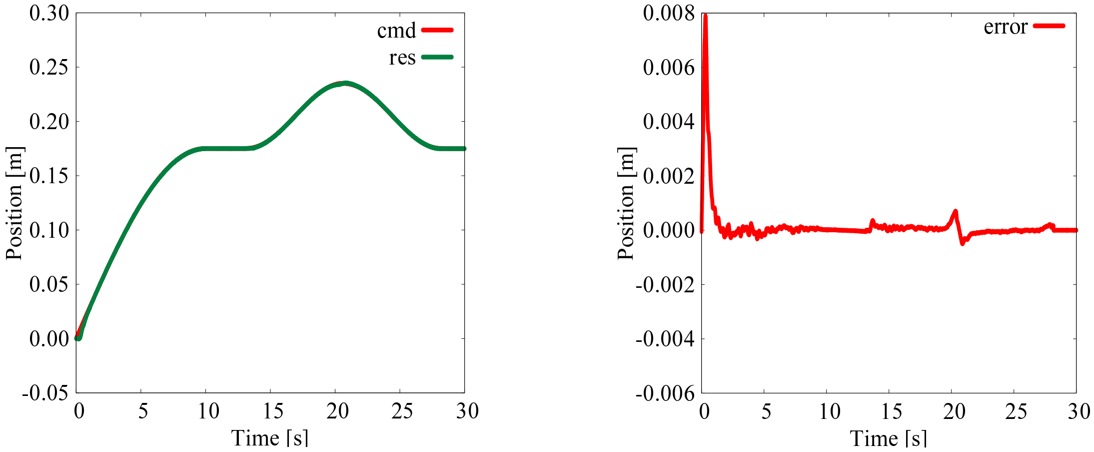

(d) Position response of y axis.

(e) Error in y axis.

Fig. 2-15: Experimental result of position response.

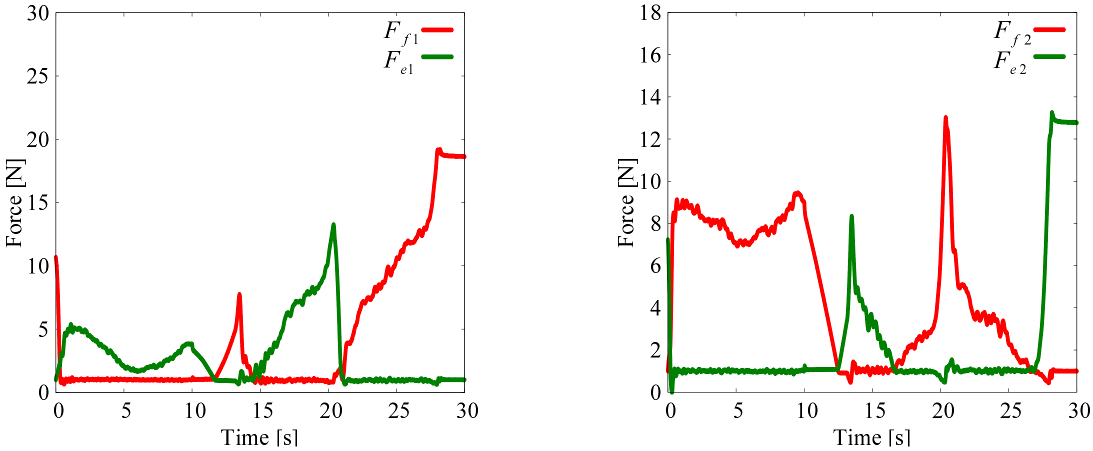

(a) Monoarticular output1.

(b) Monoarticular output2.

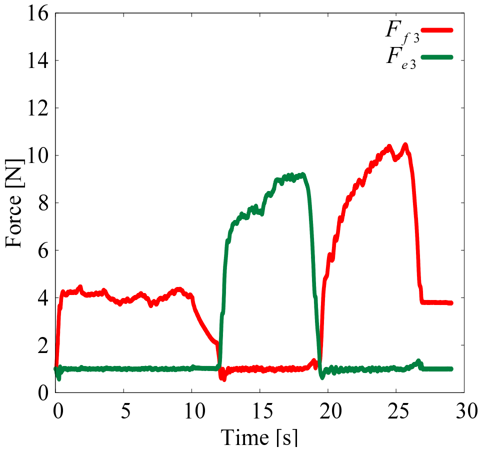

(c) Biarticular output.

Fig. 2-16: Experimental result of force response.

2.7 Summary

In this chapter, the motion control of the rotary motor and the two-link manipulator equipped with a biarticular muscle were explained. The rotary motor was modeled, and DOB for robust acceleration control and RTOB for estimating the external torque were described. The angle control and the torque control using DOB were constructed. Finally, the control method of the two-link manipulator was proposed. the validity of the proposed control system was confirmed by experiment. The biological mechanism could be accomplished by eight linear motors; therefore, a disadvantage, that the number of actuators is larger than the number of joints in biological mechanisms, was found. Thus, encoderless estimation is used to solve the problem.

Chapter 3

Angle Estimation method of Brushless DC Motor using Digital Hall Sensor and Counter EMF

3.1 Introduction

Chapter 1 introduced the different types of electric actuators. PMSMs can be classified into Interior Permanent Magnet Synchronous Motors (IPMSM) and Surface Permanent Magnet Synchronous Motors (SPMSM), as shown in Fig. 3-1. The IPMSM and SPMSM can be classified according to their mechanistic difference. The magnets of an IPMSM are buried in the rotor, while the magnets of an SPMSM are mounted on the rotor surface. The rotor structures of these PMSMs are shown in Fig. 3-2 and Fig. 3-3. These kinds of motors have differences not only in their mechanisms but also in their characteristics. The IPMSM has high saliency, whereas the SPMSM has very small saliency. The saliency is caused by fluctuations in the magnetic resistance. The IPMSM is susceptible to magnetic saturation, whereas the SPMSM is less susceptible. The IPMSM is adopted for large motors since their magnets are embedded in the rotor. For compact synchronous motors, the SPMSM is mainstream. This paper focuses on small electric motors used in home environments and in human-assist robots. Therefore, the SPMSM is discussed in this chapter.

This chapter presents an algorithm to achieve precise angle estimation using a digital Hall sensor and counter EMF. Hall sensors are widely used in applications of BLDC motor to provide phase angle information. However, the low-resolution angle information provided by the Hall sensor cannot achieve precise angle control. In the proposed method, the angle and angular velocity of the rotor are estimated

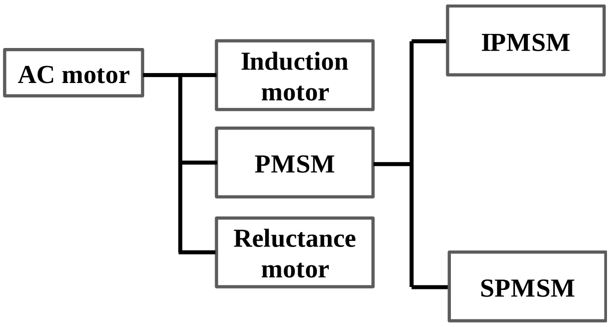

Fig. 3-1: Types of AC motor.

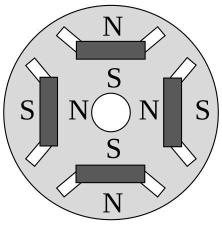

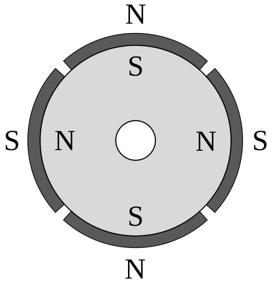

Fig. 3-2: Rotor structure of IPMSM.

Fig. 3-3: Rotor structure of SPMSM.

by combining the digital Hall sensor and counter EMF based estimation methods. This method uses Hall sensors for accurate and periodic detection of the angle. Furthermore, the interpolation between the detected angles is performed by the counter EMF. The effectiveness of the proposed approach is verified through simulations and experiments.

This chapter is organized as follows. Section 3.2 describes the modeling of BLDC motors and digital Hall sensors. Section 3.3 describes the angle estimation method and the control method for BLDC motors using counter EMF signals and Hall sensor signals. Simulations and experiments of the proposed angle estimation method are shown in Section 3.4. Finally, a summary of this chapter is provided in Section 3.5.

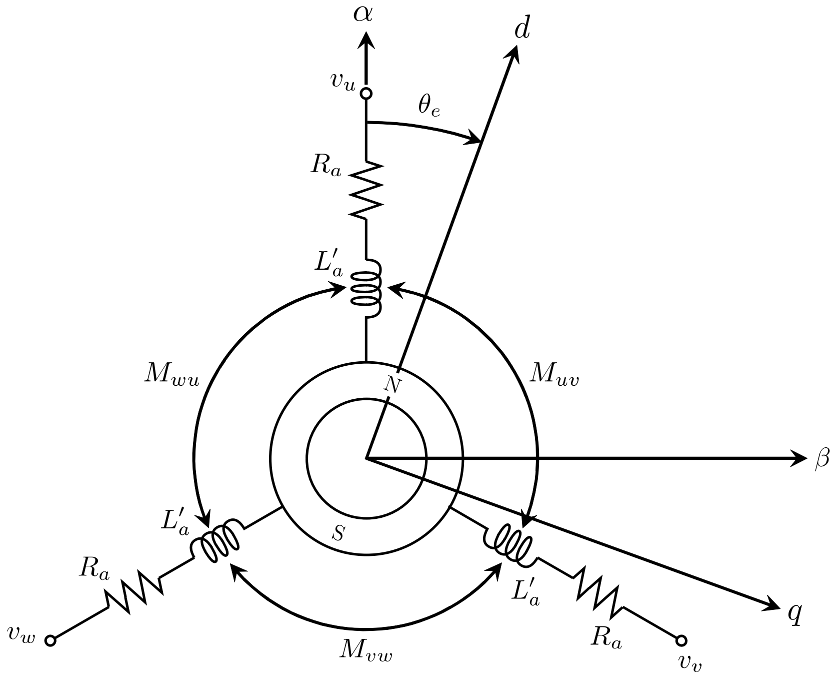

Fig. 3-4: Equivalent electrical circuit model of BLDC motor.

3.2 Modeling

3.2.1 Modeling of brushless DC motor

This chapter focuses on the three-phase surface permanent magnet BLDC motor. The equivalent electrical circuit model of a BLDC motor is shown in Fig. 3-4. the voltage equation of the model is expressed as

$$\begin{bmatrix} v_u \\ v_v \\ v_w \end{bmatrix} = \begin{bmatrix} R_a + pL_u & pM_{uv} & pM_{wu} \\ pM_{uv} & R_a + pL_v & pM_{vw} \\ pM_{wu} & pM_{vw} & R_a + pL_v \end{bmatrix} \begin{bmatrix} i_u \\ i_v \\ i_w \end{bmatrix} + \begin{bmatrix} e_u \\ e_v \\ e_w \end{bmatrix}, \tag{3.1}$$

with

$$\begin{cases} L_u = l_a + L'_a - L_m \cos 2\theta_e \\ L_v = l_a + L'_a - L_m \cos\left(2\theta_e + \dfrac{2}{3}\pi\right) \\ L_w = l_a + L'_a - L_m \cos\left(2\theta_e - \dfrac{2}{3}\pi\right) \end{cases}, \tag{3.2}$$

$$\begin{cases} M_{uv} = -\dfrac{1}{2}L'_a - L_m \cos\left(2\theta_e - \dfrac{2}{3}\pi\right) \\ M_{vw} = -\dfrac{1}{2}L'_a - L_m \cos 2\theta_e \\ M_{wu} = -\dfrac{1}{2}L'_a - L_m \cos\left(2\theta_e + \dfrac{2}{3}\pi\right) \end{cases}, \tag{3.3}$$

$$\begin{cases} e_u = \omega_e \mathit{\Psi_0} \cos 2\theta_e \\ e_v = \omega_e \mathit{\Psi_0} \cos\left(2\theta_e - \dfrac{2}{3}\pi\right) \\ e_w = \omega_e \mathit{\Psi_0} \cos\left(2\theta_e + \dfrac{2}{3}\pi\right) \end{cases}. \tag{3.4}$$

These equations are called the three-phase coordinate system. In the case of a non-salient-pole machine such as the SPMSM, the value of L_m is zero. Therefore, the inductances are not functions of the rotor angle. The three-phase coordinate system can be transformed into a stationary coordinate system, with $\alpha\beta$-axes, by using the transformation matrix ${}_{uvw}\boldsymbol{c}^{\alpha\beta}$.

$${}_{uvw}\boldsymbol{c}^{\alpha\beta} = \sqrt{\frac{2}{3}} \begin{bmatrix} 1 & -\dfrac{1}{2} & -\dfrac{1}{2} \\ 0 & \dfrac{\sqrt{3}}{2} & -\dfrac{\sqrt{3}}{2} \end{bmatrix} \tag{3.5}$$

Thus, (3.1) can be transformed into (3.6) by applying (3.5) as

$$\begin{bmatrix} v_\alpha \\ v_\beta \end{bmatrix} = \begin{bmatrix} R_a + pL_a & 0 \\ 0 & R_a + pL_a \end{bmatrix} \begin{bmatrix} i_\alpha \\ i_\beta \end{bmatrix} + \begin{bmatrix} e_\alpha \\ e_\beta \end{bmatrix}, \tag{3.6}$$

with

$$L_a = l_a + \frac{3}{2}L'_a, \tag{3.7}$$

$$\begin{cases} e_\alpha = -\omega_e \varPsi \sin\theta_e \\ e_\beta = \omega_e \varPsi \cos\theta_e \end{cases}, \tag{3.8}$$

$$\varPsi = \sqrt{\frac{3}{2}}\varPsi_0. \tag{3.9}$$

From these equations, the stationary coordinate model includes the actual angle and angular velocity information. To control the BLDC motors, a transformation from $\alpha\beta$-axes to dq-axes is required. The dq-axes are called rotational coordinates. The d-axis indicates that it is not related to torque generation. The q-axis indicates that it is related to torque generation. The stationary coordinate system can be transformed into a rotational coordinate system by using the transformation matrix ${}_{\alpha\beta}\boldsymbol{c}^{dq}$.

$${}_{\alpha\beta}\boldsymbol{c}^{dq} = \begin{bmatrix} \cos\theta_e & -\sin\theta_e \\ \sin\theta_e & \cos\theta_e \end{bmatrix} \tag{3.10}$$

Thus, (3.6) can be transformed into (3.11) by applying (3.10) as

$$\begin{bmatrix} v_d \\ v_q \end{bmatrix} = \begin{bmatrix} R_a + pL_d & -\omega_e L_q \\ \omega_e L_d & R_a + pL_q \end{bmatrix} \begin{bmatrix} i_d \\ i_q \end{bmatrix} + \begin{bmatrix} 0 \\ \omega_e \varPsi \end{bmatrix}, \tag{3.11}$$

where

$$L_d = L_q = L_a. \tag{3.12}$$

Finally, the torque generated by the BLDC motor is expressed as follows.

$$\begin{aligned} T_a &= \varPsi_0 \left\{ -i_u \sin\theta_e - i_v \sin\left(\theta_e - \frac{2}{3}\pi\right) - i_w \sin\left(\theta_e + \frac{2}{3}\pi\right) \right\} && (3.13) \\ &= \varPsi \left\{ -i_\alpha \sin\theta_e + i_\beta \cos\theta_e \right\} && (3.14) \\ &= \varPsi i_q && (3.15) \end{aligned}$$

3.2.2 Hall sensor

In many practical applications, three digital Hall sensors are mounted on the three-phase BLDC motor. As shown in Fig. 3-5, the Hall sensor signals are generated by the motion of the BLDC motor. The signal of one Hall sensor is repeated high and low every 180 electrical degrees. During the operation

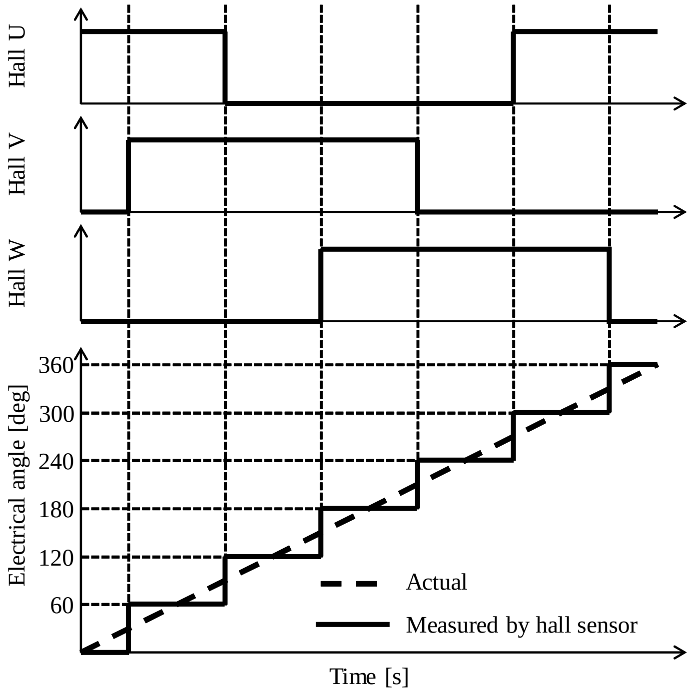

Fig. 3-5: Angle generation from digital Hall signals.

of the BLDC motor, the waveforms of the output signals can be divided into six sectors of 60 electrical degrees, because the Hall sensors are placed 120 electrical degrees apart. Therefore, three digital Hall sensors can provide the electrical angle of the BLDC motor with a resolution of 60 electrical degrees.

3.3 Angle Control Method for BLDC Motor

The angle control method for the BLDC motor is described in this section. The counter EMF observer (CFOB)-based angular velocity estimation method[29, 30] is explained in 4.3.1. Thereafter, the angle control method based on Hall sensors and counter EMF is described in 3.3.2.

3.3.1 CFOB-based angular velocity estimation for BLDC motor

From (3.6) and (3.8), the current in the $\alpha\beta$-axes is derived as

$$i_\alpha = \frac{1}{R_a + pL_a} (v_\alpha - e_\alpha), \tag{3.16}$$

$$i_\beta = \frac{1}{R_a + pL_a} (v_\beta - e_\beta). \tag{3.17}$$

In a real control system, the supply voltages v_α and v_β are calculated by the current controller as voltage references v_α^{ref} and v_β^{ref}, respectively, and the phase currents are measured by the current sensors as the current responses i_α^{res} and i_β^{res}. The motor parameters fluctuate from the nominal values due to modeling error, temperature alteration, etc. Therefore, the motor parameters are described by (3.18) and (3.19).

$$R_a = R_{an} + \Delta R_a \tag{3.18}$$

$$L_a = L_{an} + \Delta L_a \tag{3.19}$$

Here, the subscript n denotes the nominal value. Therefore, (3.16) and (3.17) can be rewritten as

$$i_\alpha^{res} = \frac{1}{R_{an} + pL_{an}} \left(v_\alpha^{ref} - v_\alpha^{dis} \right), \tag{3.20}$$

$$i_\beta^{res} = \frac{1}{R_{an} + pL_{an}} \left(v_\beta^{ref} - v_\beta^{dis} \right), \tag{3.21}$$

where

$$v_\alpha^{dis} = \frac{\Delta R_a + p\Delta L_a}{R_a + pL_a} v_\alpha^{ref} + \frac{R_{an} + pL_{an}}{R_a + pL_a} e_\alpha, \tag{3.22}$$

$$v_\beta^{dis} = \frac{\Delta R_a + p\Delta L_a}{R_a + pL_a} v_\beta^{ref} + \frac{R_{an} + pL_{an}}{R_a + pL_a} e_\beta. \tag{3.23}$$

CFOB estimates the counter EMF and the voltage disturbance, as shown in Fig. 3-6. Moreover, the angular velocity can be calculated by the estimated counter EMF and interlinkage magnet flux. From

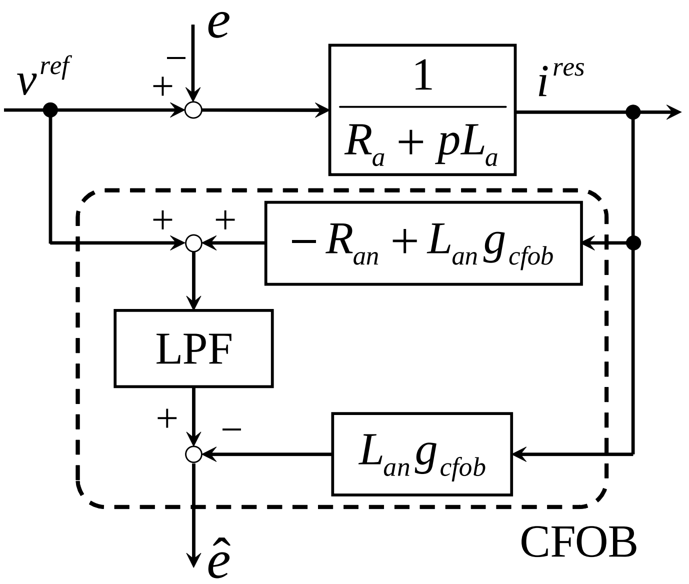

Fig. 3-6: Counter electromotive force observer.

Fig. 3-6, the estimated counter EMF is calculated by

$$\frac{1}{\Psi_n}\hat{e}_\alpha = \frac{1}{\Psi_n}\mathrm{LPF}\left[v_\alpha^{dis}\right], \tag{3.24}$$

$$= \mathrm{LPF}\Bigg[\frac{1}{\Psi_n}\frac{\Delta R_a + p\Delta L_a}{R_a + pL_a}v_\alpha^{ref} + \frac{\Psi}{\Psi_n}\frac{R_{an} + pL_{an}}{R_a + pL_a}e_\alpha\Bigg], \tag{3.25}$$

$$= -\hat{\omega}_e^{res}\sin\theta_e, \tag{3.26}$$

$$\frac{1}{\Psi_n}\hat{e}_\beta = \frac{1}{\Psi_n}\mathrm{LPF}\left[v_\beta^{dis}\right], \tag{3.27}$$

$$= \mathrm{LPF}\Bigg[\frac{1}{\Psi_n}\frac{\Delta R_a + p\Delta L_a}{R_a + pL_a}v_\beta^{ref} - \frac{\Psi}{\Psi_n}\frac{R_{an} + pL_{an}}{R_a + pL_a}e_\beta\Bigg], \tag{3.28}$$

$$= \hat{\omega}_e^{res}\cos\theta_e. \tag{3.29}$$

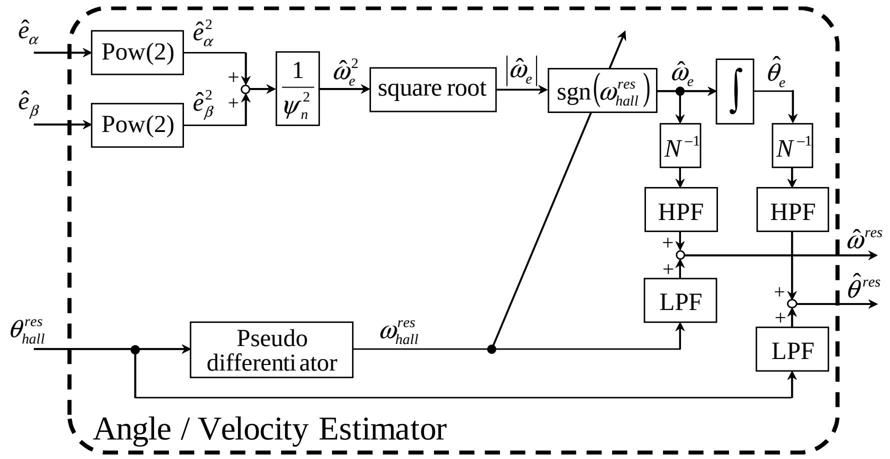

Fig. 3-7: Angle/velocity estimator for BLDC motor.

From these equations, the absolute value of angular velocity is derived as

$$
\begin{aligned}
|\hat{\omega}_e^{res}| &= \sqrt{(-\hat{\omega}_e^{res})^2 \sin^2\theta_e + (\omega_e^{res})^2 \cos^2\theta_e}, \\
&= \sqrt{\left(\frac{1}{\Psi_n}\hat{e}_\alpha\right)^2 + \left(\frac{1}{\Psi_n}\hat{e}_\beta\right)^2}, \qquad (3.30) \\
&= \sqrt{\frac{1}{\Psi_n^2}\left(\hat{e}_\alpha^2 + \hat{e}_\beta^2\right)}. \qquad (3.31)
\end{aligned}
$$

When the modeling error and parameter fluctuations are sufficiently small, CFOB can estimate the absolute value of angular velocity without any angle sensors. However, CFOB cannot estimate around the zero-speed region because of the signal-to-noise ratio degradation. Furthermore, the rotational direction cannot be determined.

3.3.2 Angle and velocity estimation by Hall sensor and CFOB

The angle and angular velocity estimation method for the BLDC motor based on a Hall sensor and CFOB are described in this section. Accurate angle information can be obtained, and high-performance operation can be achieved. In the proposed method, the angle and angular velocity are estimated by combining the digital Hall sensor and CFOB. This method can accurately detect the angle periodically by digital Hall sensor. Furthermore, interpolation between the detected angles is performed by the counter EMF. The block diagram of the proposed estimation method is shown in Fig. 3-7. In this method, the absolute value of the electrical angle is calculated by (3.30). Subsequently, the rotational direction is

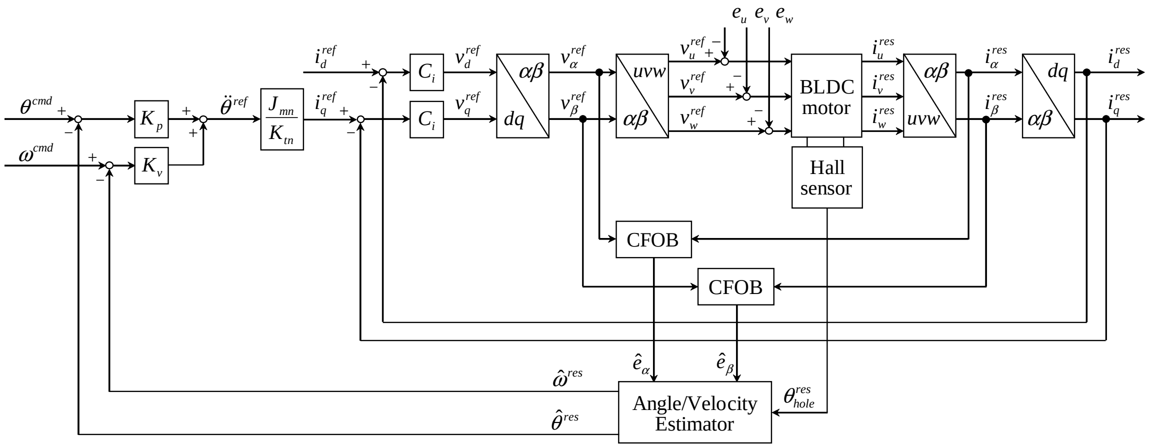

Fig. 3-8: Whole block diagram of proposed control system.

determined by the angular velocity response from the Hall sensor. The estimated angular velocity is derived as

$$\hat{\omega}^{res} = \mathrm{LPF}\left[\omega_{hall}^{res}\right] + \mathrm{HPF}\left[\frac{1}{N}\hat{\omega}_e\right]. \tag{3.32}$$

Here, N denotes the number of pole pairs. Moreover, the estimated angle is derived as

$$\hat{\theta}^{res} = \mathrm{LPF}\left[\theta_{hall}^{res}\right] + \mathrm{HPF}\left[\frac{1}{N}\hat{\theta}_e\right]. \tag{3.33}$$

In these equations, the LPF cut out the sudden change in signals, because of low resolution. The HPF cut out the zero-point shifting and the drift phenomenon caused by modeling errors and parameter variations. Finally, a whole block diagram of the proposed control system is shown in Fig. 3-8. Here, the current controller is a proportional-integral controller, and the dq-axes current references are expressed as

$$i_d^{ref} = 0, \tag{3.34}$$

$$i_q^{ref} = \frac{J_{mn}}{K_{tn}}\left\{K_p\left(\theta^{cmd} - \hat{\theta}^{res}\right) + K_v\left(\omega^{cmd} - \hat{\omega}^{res}\right)\right\}. \tag{3.35}$$

3.4 Simulations and Experiments

3.4.1 Outline of simulations and Experiments

The parameters utilized in simulations are shown in Table 3.1. These parameters are assumed for the surface permanent magnet BLDC motor “MDH-7018” made by Microtech Laboratory Inc. This

Table 3.1: Parameters utilized in simulations

Symbol	Meanings of the parameter	Value
J_m	Actual moment of inertia	$8.6\times10^{-5}\mathrm{kg}\cdot\mathrm{m}^2$
Ψ	Actual EMF/torque constant	0.3 Nm/A or V/(rad/s)
R_a	Actual resistance	2.4 Ω
L_u, L_v, L_w	Actual inductance of each coil	3.0 mH
L_d, L_q	Actual inductance in dq-axes	4.0 mH
K_p	Proportional gain	6400 $1/s^2$
K_v	Derivative gain	160 $1/s$
K_{ii}	Integral gain of C_i	10
K_{pi}	Proportional gain of C_i	200
N	Number of pole pairs	10
–	Cutoff frequency of CFOB	1000 rad/s
–	Cutoff frequency of LPF	50 rad/s
–	Cutoff frequency of HPF	50 rad/s
–	Cutoff frequency of pseudo differentiator	500 rad/s

section describes the confirmation of the validity of the proposed control method. The purposes of the simulations are to compare the performance and robustness against the modeling error of the counter EMF-based method, the method using Hall sensor response, and the proposed method. As mentioned in section 4.3.1, EMF-based angular velocity estimation cannot determine the rotational direction. However, to compare the performance, it is assumed in this simulation that the actual rotational direction can be identified. Furthermore, to confirm the robustness of the modeling error, the nominal value of Ψ that indicates the counter EMF constant and torque constant was changed by 10 $\%$ from the actual value.

3.4.2 Simulation of angle estimation

This section shows the angle estimation results of the counter EMF-based control method, the control method using the Hall sensor response, and the proposed method. The estimation results are shown in Fig. 3-9 to 3-17. In these figures, the red solid line, black dashed line, blue chain line, and green dotted line denote the command value, actual value, estimated value, and error between the actual and estimated values, respectively. From Fig. 3-9, 3-12, and 3-15, the counter EMF-based method could estimate the angle with high accuracy when the modeling error was zero. However, when the modeling error existed, the estimation accuracy by the counter EMF-based method deteriorated. From Fig. 3-10, 3-13 and 3-16, in the method using the Hall sensor, the estimation accuracy was not affected by modeling error. From Fig. 3-11, 3-14 and 3-17, the proposed method achieved highly accurate angle estimation regardless of the modeling error.

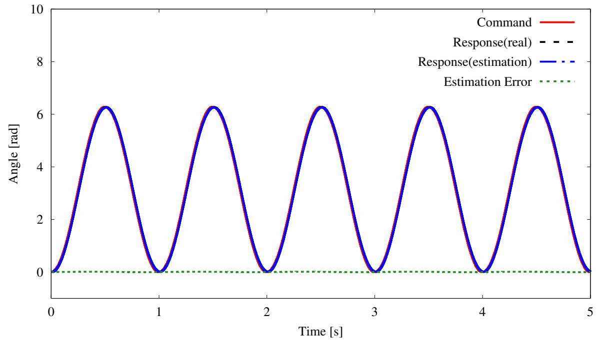

(a) Angular response

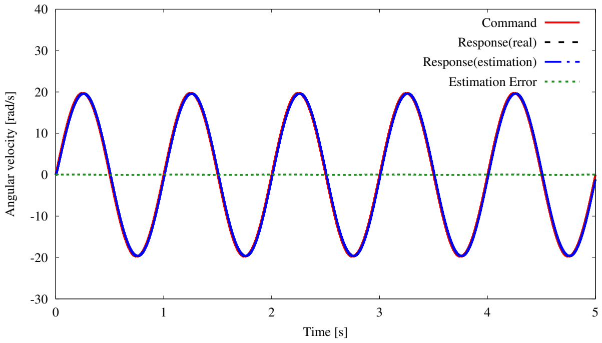

(b) Angular velocity response

Fig. 3-9: Estimation result of counter EMF-based method. ($\Psi_n = 1.0\,\Psi$)

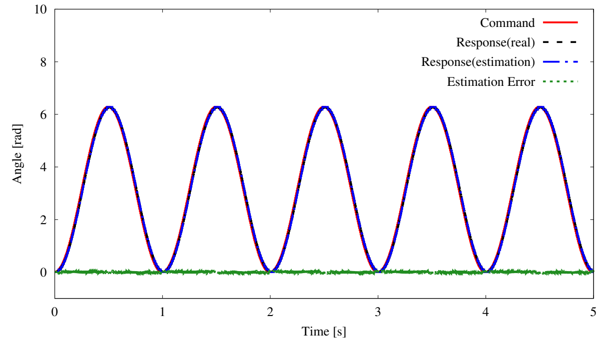

(a) Angular response

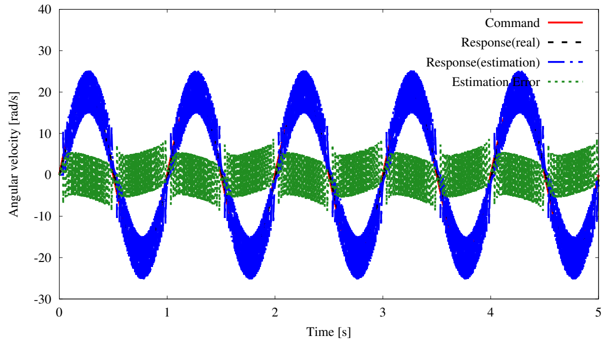

(b) Angular velocity response

Fig. 3-10: Estimation result by using Hall sensor response. ($\Psi_n = 1.0\,\Psi$)

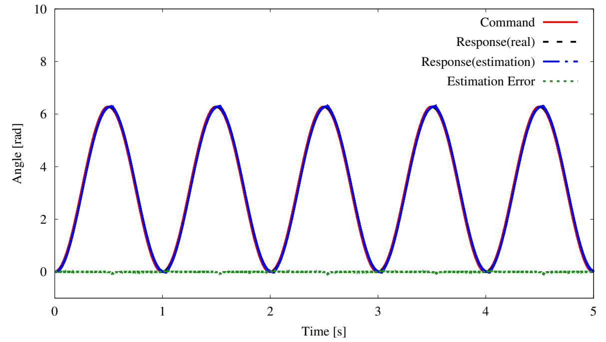

(a) Angular response

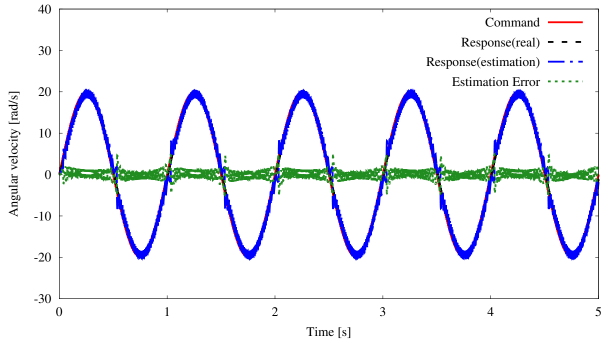

(b) Angular velocity response

Fig. 3-11: Estimation result of proposed method. ($\Psi_n = 1.0\,\Psi$)

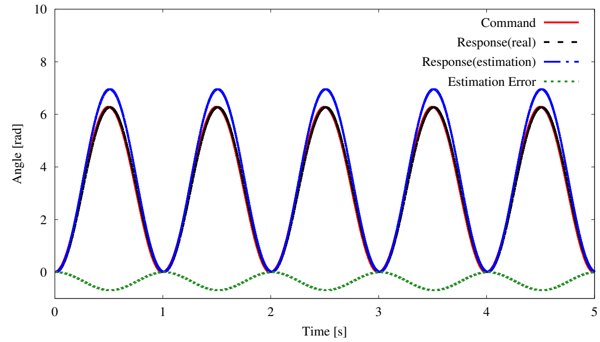

(a) Angular response

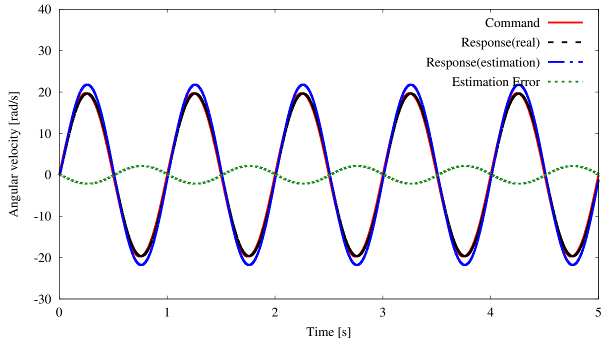

(b) Angular velocity response

Fig. 3-12: Estimation result of counter EMF-based method. ($\Psi_n = 0.9\,\Psi$)

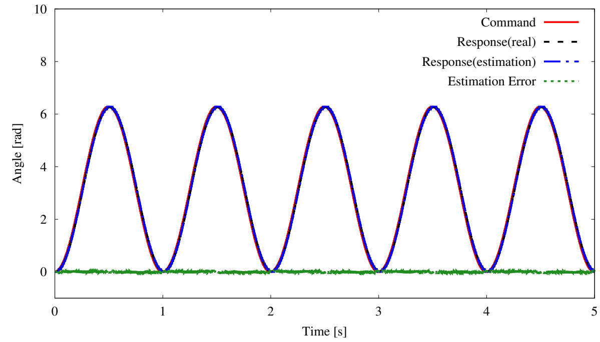

(a) Angular response

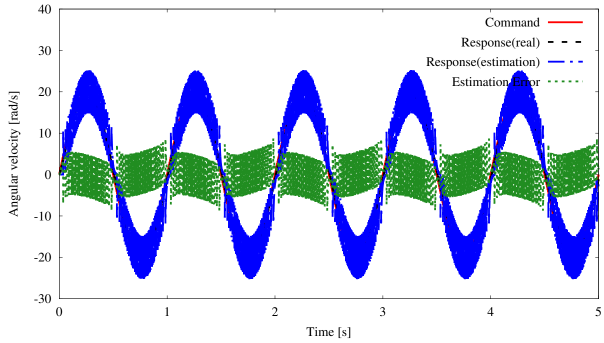

(b) Angular velocity response

Fig. 3-13: Estimation result by using Hall sensor response. ($\Psi_n = 0.9\,\Psi$)

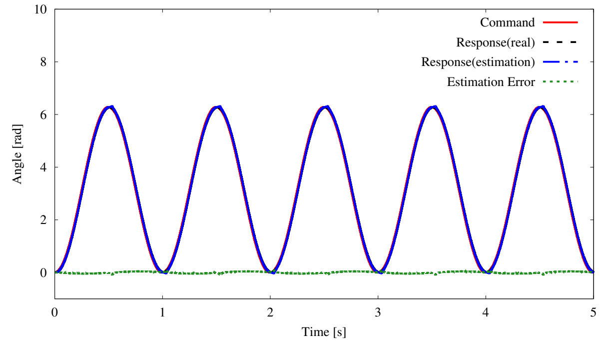

(a) Angular response

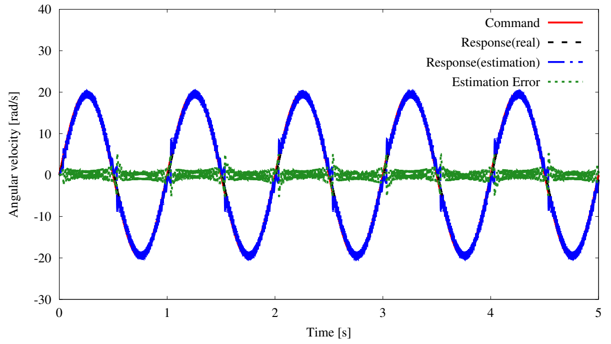

(b) Angular velocity response

Fig. 3-14: Estimation result of proposed method. ($\Psi_n = 0.9\,\Psi$)

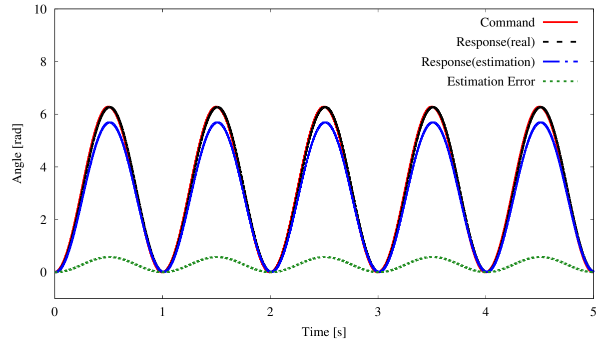

(a) Angular response

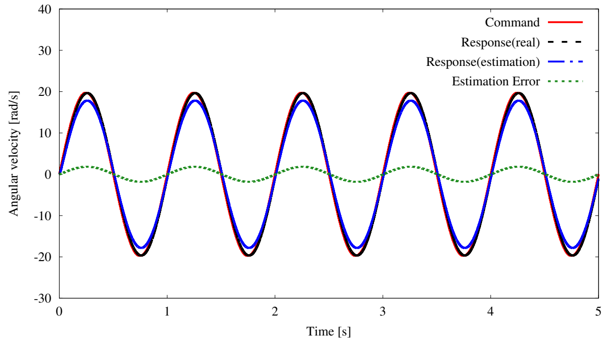

(b) Angular velocity response

Fig. 3-15: Estimation result of counter EMF-based method. ($\Psi_n = 1.1\,\Psi$)

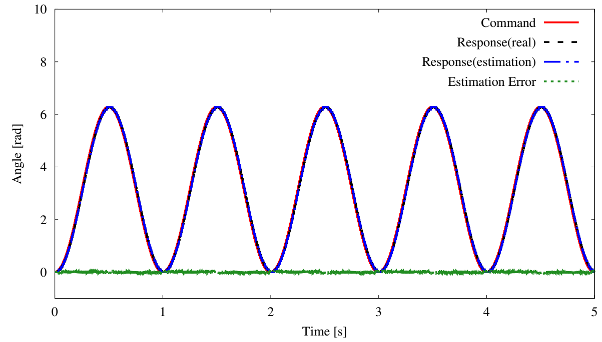

(a) Angular response

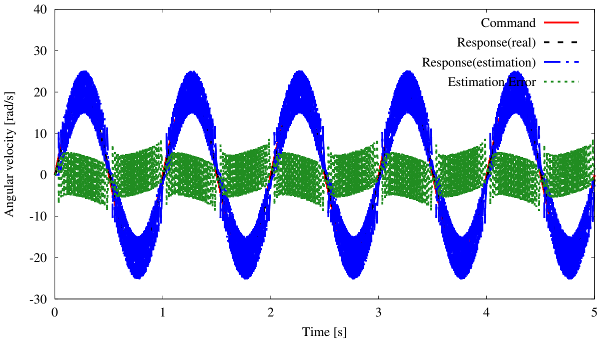

(b) Angular velocity response

Fig. 3-16: Estimation result by using Hall sensor response. ($\Psi_n = 1.1\,\Psi$)

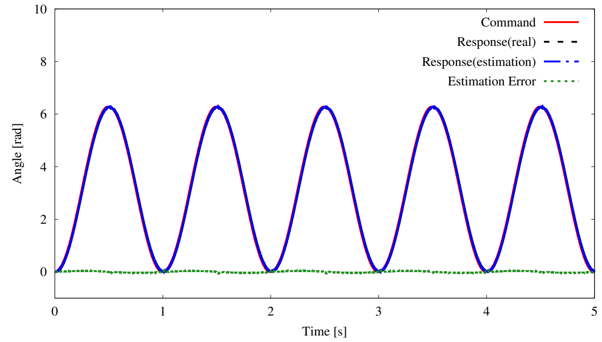

(a) Angular response

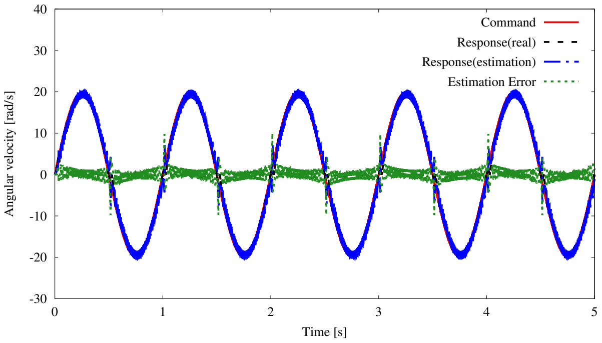

(b) Angular velocity response

Fig. 3-17: Estimation result of proposed method. ($\Psi_n = 1.1\,\Psi$)

3.4.3 Simulation of angle control

This section shows the simulation results of angle control using the counter EMF-based control method, the control method using the Hall sensor response, and the proposed method. The simulation results are shown in Fig. 3-18 to 3-26. As in section 3.4.2, the red solid line, black dashed line, blue chain line, and green dotted line denote the command value, actual value, estimated value, and error between the actual and estimated values, respectively.

From Fig. 3-18, 3-19, and 3-20, the counter EMF-based method showed the highest performance in a situation without modeling error. However, the counter EMF-based method was weak against modeling errors, as seen in Fig. 3-21 and 3-24. From Fig. 3-19, 3-22, and 3-25, there was no influence observed from modeling error on the control method using the Hall sensor response. However, the angular velocity response was very oscillatory due to the pseudo-differentiator in the low-resolution sensor. If the cutoff frequency of the pseudo differentiator decreased in order to reduce the vibration of the angular velocity response, phase lag of the angle occurs and control becomes impossible. Finally, from Fig. 3-20, 3-23, and 3-26, the proposed method achieved the highest control performance. Furthermore, the robustness against modeling errors was also confirmed.

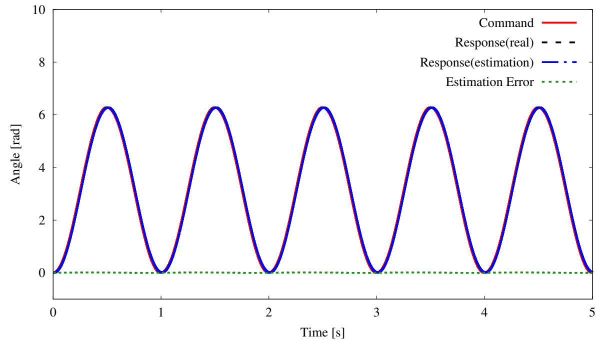

(a) Angular response

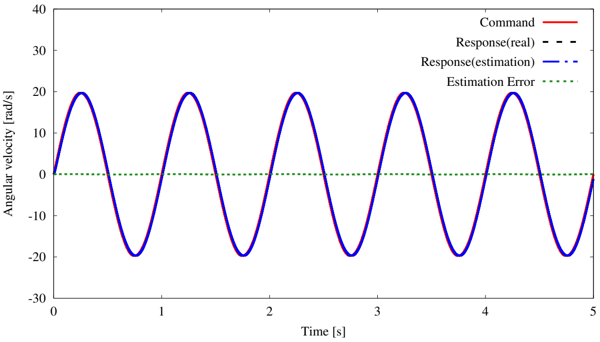

(b) Angular velocity response

Fig. 3-18: Simulation result of counter EMF-based method. ($\Psi_n = 1.0\,\Psi$)

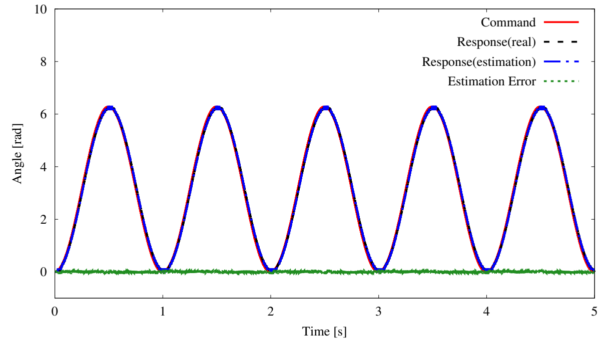

(a) Angular response

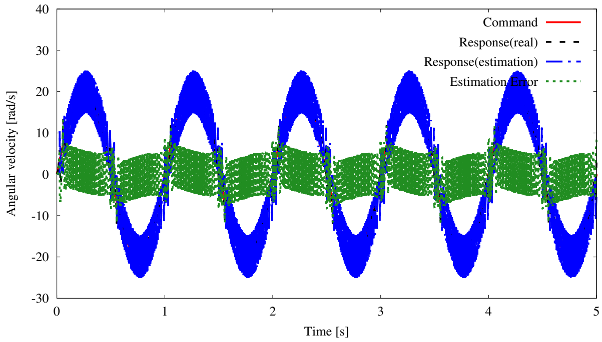

(b) Angular velocity response

Fig. 3-19: Simulation result by using Hall sensor response. ($\Psi_n = 1.0\,\Psi$)

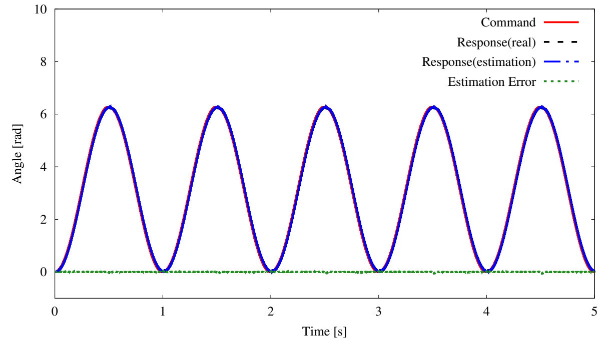

(a) Angular response

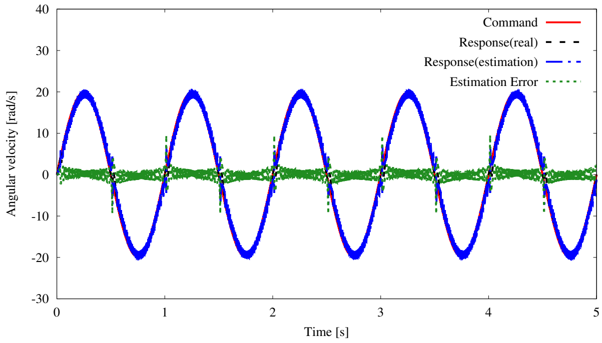

(b) Angular velocity response

Fig. 3-20: Simulation result of proposed method. ($\Psi_n = 1.0\,\Psi$)

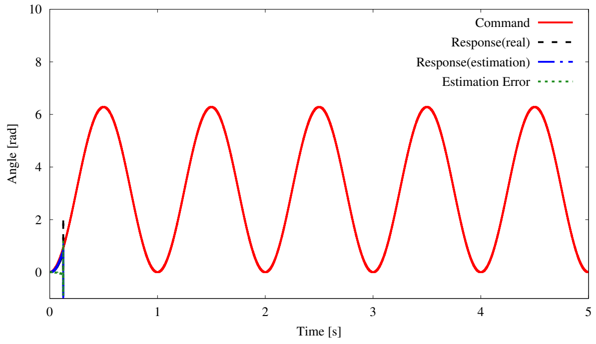

(a) Angular response

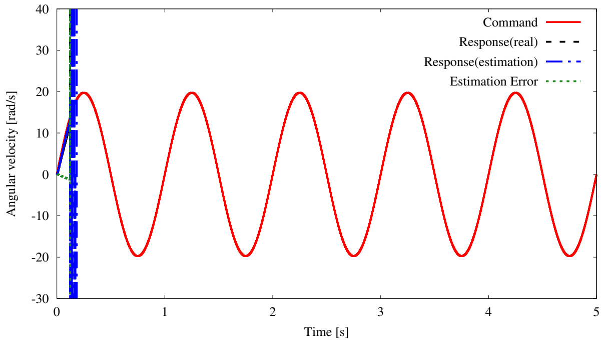

(b) Angular velocity response

Fig. 3-21: Simulation result of counter EMF-based method. ($\Psi_n = 0.9\,\Psi$)

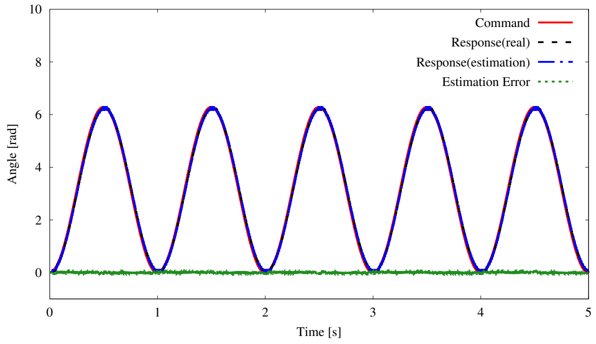

(a) Angular response

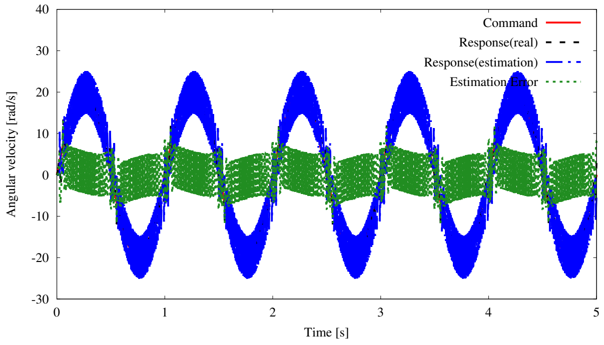

(b) Angular velocity response

Fig. 3-22: Simulation result by using Hall sensor response. ($\Psi_n = 0.9\,\Psi$)

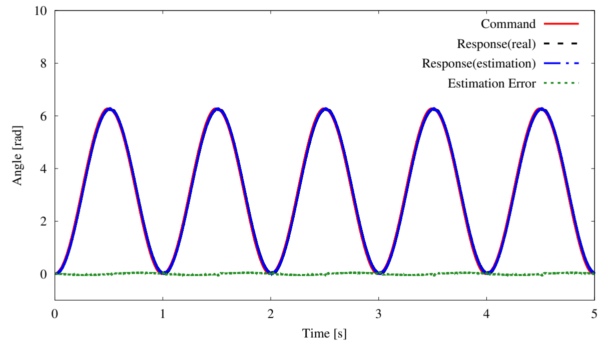

(a) Angular response

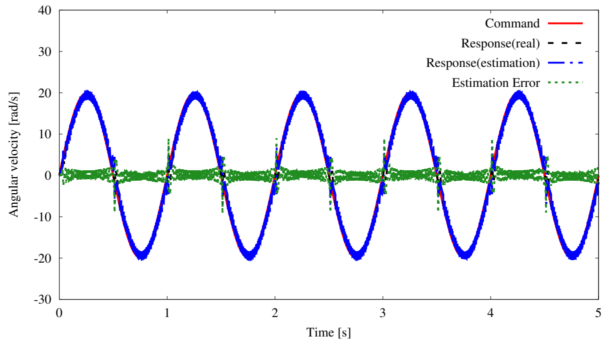

(b) Angular velocity response

Fig. 3-23: Simulation result of proposed method. ($\varPsi_n = 0.9\,\varPsi$)

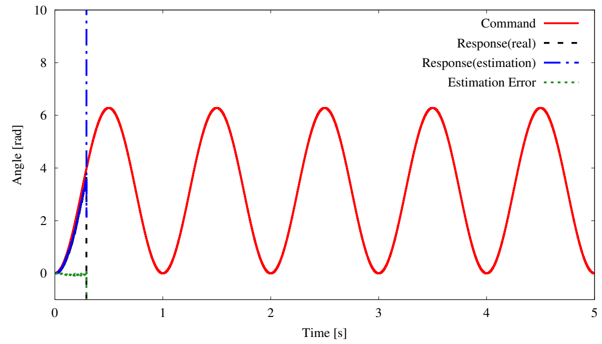

(a) Angular response

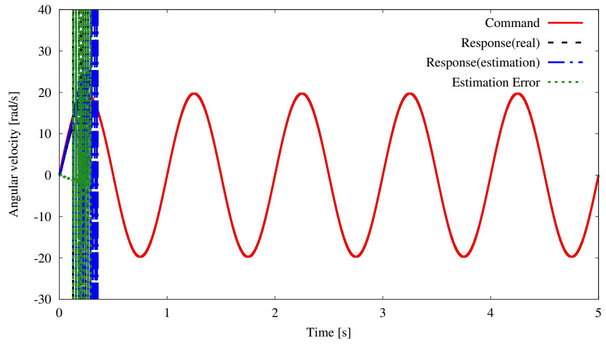

(b) Angular velocity response

Fig. 3-24: Simulation result of counter EMF-based method. ($\varPsi_n = 1.1\,\varPsi$)

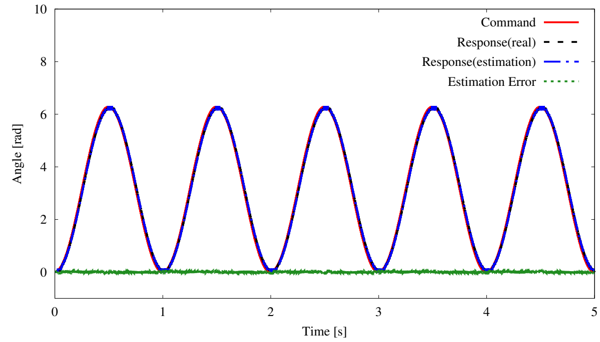

(a) Angular response

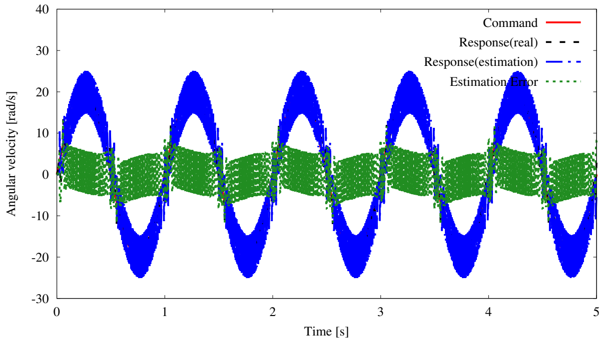

(b) Angular velocity response

Fig. 3-25: Simulation result by using Hall sensor response. ($\Psi_n = 1.1\,\Psi$)

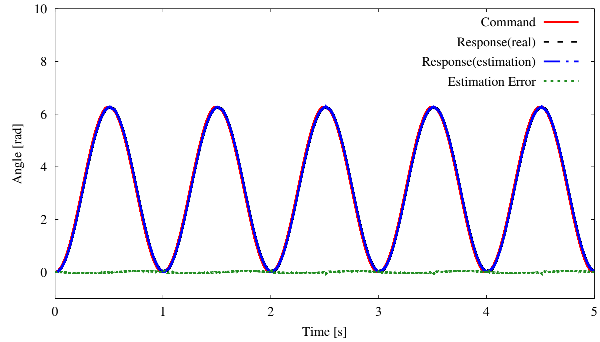

(a) Angular response

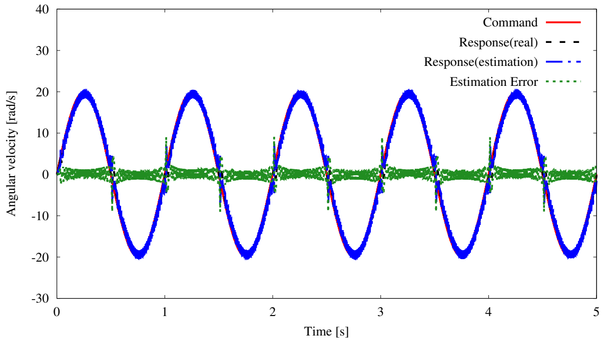

(b) Angular velocity response

Fig. 3-26: Simulation result of proposed method. ($\Psi_n = 1.1\,\Psi$)

Table 3.2: Parameters utilized in experiments

Symbol	Meanings of the parameter	Value
J_{mn}	Nominal moment of inertia	$8.6\times10^{-5}\mathrm{kg}\cdot\mathrm{m}^2$
Ψ_n	Nominal EMF/torque constant	0.3 Nm/A or V/(rad/s)
R_{an}	Nominal resistance	2.4 Ω
L_{un}, L_{vn}, L_{wn}	Nominal inductance of each coil	3.0 mH
L_{dn}, L_{qn}	Nominal inductance in dq-axes	4.0 mH
K_p	Proportional gain	6400 $1/s^2$
K_v	Derivative gain	160 $1/s$
K_{ii}	Integral gain of C_i	10
K_{pi}	Proportional gain of C_i	200
N	Number of pole pairs	10
–	Cutoff frequency of CFOB	1000 rad/s
–	Cutoff frequency of LPF	50 rad/s
–	Cutoff frequency of HPF	50 rad/s
–	Cutoff frequency of pseudo differentiator	500 rad/s

3.4.4 Experiment of angle estimation

In this section, the validity of the proposed estimation method is confirmed by experimental results. The parameters utilized in experiments are shown in Table 3.2. The experimental results are shown from Fig. 3-27 to 3-29. As in simulations, the red solid line, black dashed line, blue chain line, and green dotted line denote the command value, actual value, estimated value, and error between the actual and estimated values, respectively. As seen in Fig. 3-27, estimation error occurred in the counter EMF-based method. Furthermore, the drift phenomenon was confirmed in the angle estimation result. In an actual system, the modeling error cannot be reduced to zero. Therefore, the estimation error cannot be eliminated. From Fig. 3-28, the actual angle was detected in the method using the Hall sensor. However, a large estimation error existed in the angular velocity, which was caused by the pseudo-differentiator in the low-resolution sensor. Finally, from Fig. 3-29, the proposed method achieved accurate angle estimation. Angular velocity estimation was also possible; although a slight error occurred, an actual value could be roughly estimated.

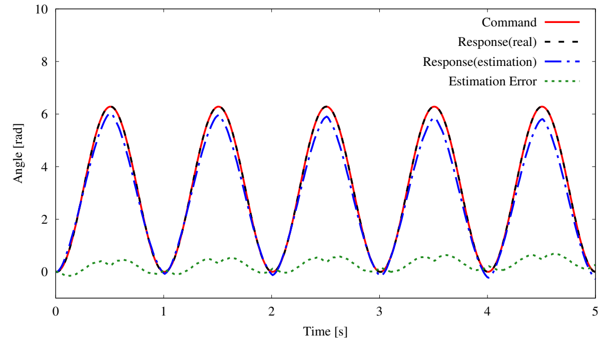

(a) Angular response

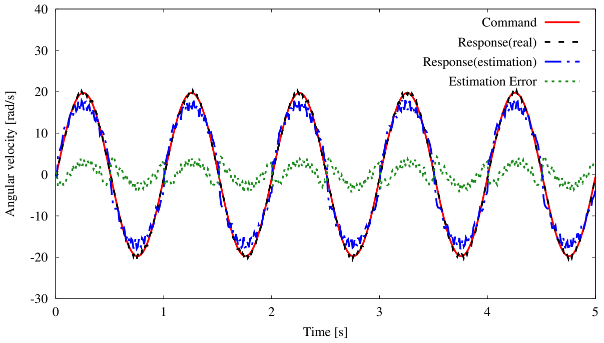

(b) Angular velocity response

Fig. 3-27: Experimental result of counter EMF-based method.

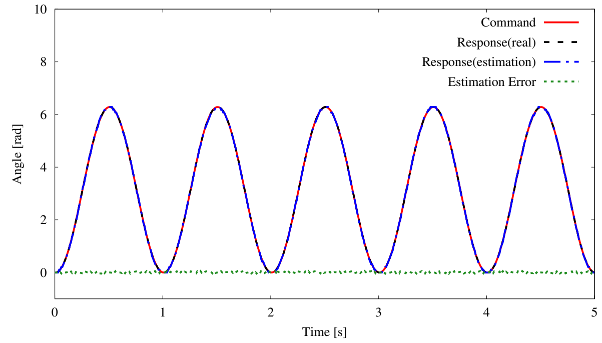

(a) Angular response

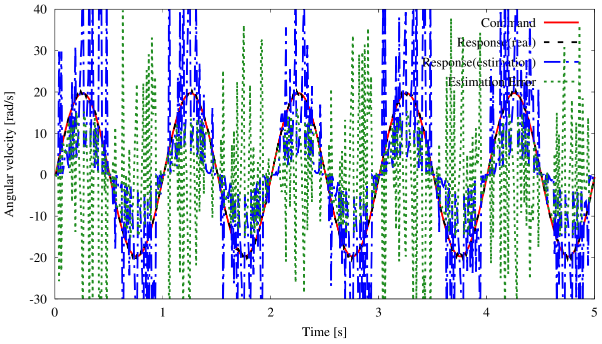

(b) Angular velocity response

Fig. 3-28: Experimental result by using Hall sensor response.

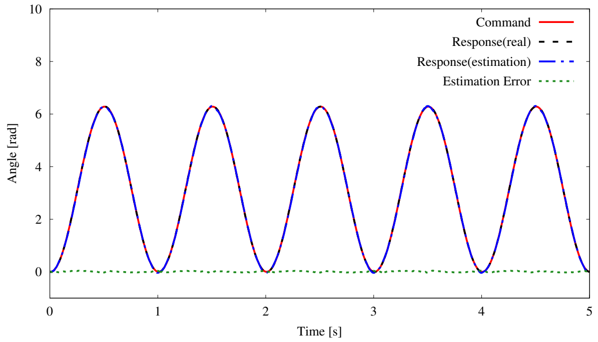

(a) Angular response

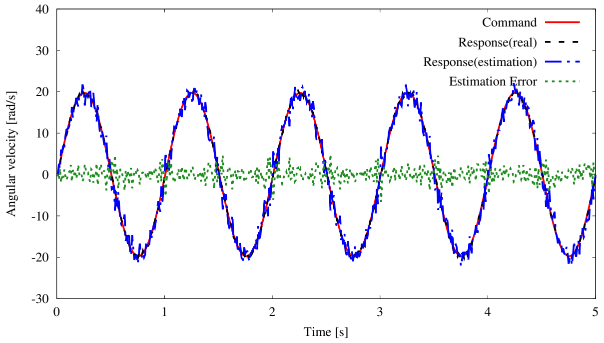

(b) Angular velocity response

Fig. 3-29: Experimental result of proposed method.

3.5 Summary

In this chapter, an algorithm to achieve a precise angle estimation for the BLDC motor using the digital Hall sensor and counter EMF was proposed. The validity of the proposed method was confirmed by using simulations and experiments. Based on the results, the proposed method could achieve high-performance angle estimation in comparison with other methods. Furthermore, robustness against modeling errors was also confirmed.

Chapter 4

Sensorless Angle Estimation for Brushed DC Motor using Impedance Variation

4.1 Introduction

The BDC motor can be classified precisely, as shown in Fig 4-1. First, the BDC motor can be classified as a winding-field DC motor or a permanent-magnet DC motor. In the past, the winding-field DC motor was mainstream. However, the permanent magnet DC motor is now predominant due to the performance improvement realized with permanent magnets. The permanent-magnet DC motor can also be classified into those with even numbers of slots and odd numbers of slots. In the case of the even-slots DC motor, a driving torque from the outside is required at the start of operation. The rotating direction also differs depending on the direction of the torque at the start time. This feature is not suitable for control around the zero-speed region. In the odd-slots BDC motor, the rotation direction is uniquely determined by the voltage polarity. For these reasons, in the field of small actuators, the odd-slots BDC motor is widely used. Therefore, this chapter focuses on the odd-slots BDC motor.

A sensorless angle estimation method for the BDC motor is proposed in this chapter. In order to estimate the angle of the rotor without any mechanical sensors, the proposed method uses the impedance variation via contact switching. In typical sensorless angle estimation methods, the angle of the rotor is estimated by the counter EMF. However, methods based on the counter EMF cannot estimate the angle accurately during standstill or at low speeds. Furthermore, estimation errors occur due to the modeling error. In the proposed method, the angle of the rotor is estimated using the angle-dependent impedance. The impedance is measured by high-frequency signal injection and synchronous detection. This method

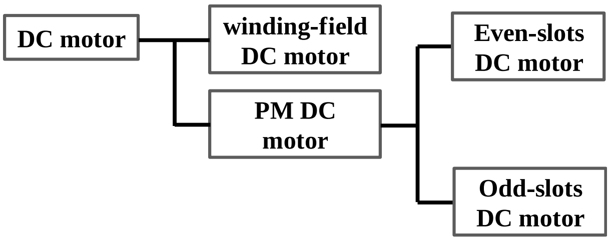

Fig. 4-1: Types of BDC motor.

can be used to estimate the angle of the rotor directly. Therefore, it is possible to estimate the angle accurately at low speeds. The validity of the proposed method is verified through experiments.

This chapter is organized as follows. Section 4.2 describes the modeling of the BDC motor. Next, section 4.3 describes the angle estimation method for the BDC motor with an odd number of slots based on counter EMF and position-dependent impedance. Experiments on the conventional and proposed methods are shown in section 4.4. Finally, this chapter is concluded in section 4.5.

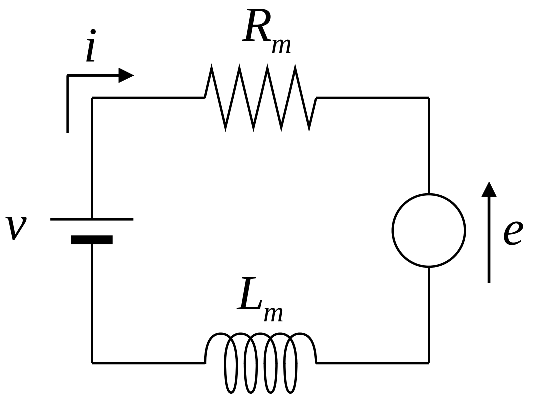

Fig. 4-2: Electrical system of brushed DC motor.

4.2 Modeling of Brushed DC Motor

This chapter focuses on the permanent-magnet BDC motor. The electrical system of the BDC motor is shown in Fig. 4-2, in which the circuit equation is expressed as

$$v = R_m i + L_m \frac{di}{dt} + e, \tag{4.1}$$

with

$$e = K_e \dot{\theta}, \tag{4.2}$$

where v is the applied voltage to the BDC motor, i is the current flowing through the BDC motor, e is the counter EMF, R_m and L_m are the resistance and inductance of the BDC motor, respectively, K_e is the counter EMF constant, and $\dot{\theta}$ is the angular velocity of the BDC motor. As expressed in (4.2), the counter EMF is dependent on angular velocity. Therefore, conventional methods estimate the angular velocity by using the counter EMF[30]. The mechanical system of the BDC motor, considering the electrical system, is expressed as

$$J_m \ddot{\theta} = K_t i - T_{load}. \tag{4.3}$$

Here, J_m is the inertia of the BDC motor, K_t is the torque constant, T_{load} is the load torque, and $\ddot{\theta}$ is the angular acceleration.

In a practical system, the rotor of the BDC motor consists of some number of slots. In particular, small

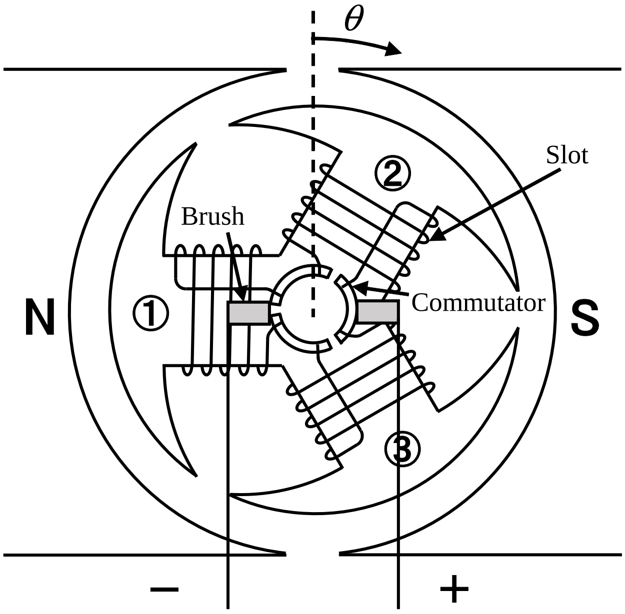

Fig. 4-3: 3-slots concentrated-winding brushed DC motor.

BDC motors have odd numbers of slots in order to uniquely determine the rotational direction due to the applied voltage. For example, the mechanism of the 3-slots concentrated-winding BDC motor is shown in Fig. 4-3.

In the BDC motor, because the direction of the current flowing through each armature winding changes in accordance with the switching of the contacts between the brush and the commutator, torque is always generated. Ignoring the change in magnetic flux due to the current change for simplicity, and considering only the magnetic flux of the permanent magnet. The flux linkage of each armature winding is expressed by

$$\Phi_1 = B_0 \cos\theta, \tag{4.4}$$

$$\Phi_2 = B_0 \cos\left(\theta + \frac{2}{3}\pi\right), \tag{4.5}$$

$$\Phi_3 = B_0 \cos\left(\theta - \frac{2}{3}\pi\right). \tag{4.6}$$

Here, B_0 is the maximum value of interlinkage magnetic flux, Φ_1, Φ_2, Φ_3 are the interlinkage magnetic flux of coil 1, 2, and 3, respectively. The mutual inductance contributing to the output torque of the motor fluctuates with the increase/decrease of the absolute value of the interlinkage magnetic flux, and influences the torque ripple. Furthermore, the influence of interlinkage magnetic flux affects not only the mutual inductance, but also the leakage inductance appearing on the equivalent circuit of the motor. Therefore, the inductance value of each coil is derived as

$$\begin{aligned} L_1 &= L_0 - L_a \cos(2\theta), && (4.7) \\ L_2 &= L_0 - L_a \cos\left\{2\left(\theta + \frac{2}{3}\pi\right)\right\}, && (4.8) \\ L_3 &= L_0 - L_a \cos\left\{2\left(\theta - \frac{2}{3}\pi\right)\right\}, && (4.9) \end{aligned}$$

where L_0 is the average value of inductance variation, L_a is the maximum value of the variation range of inductance, and L_1, L_2, and L_3 are the inductance value of each coil, respectively. In consideration of magnetic saturation, L_0 and L_a fluctuate depending on the current. However, in the use situation of an actual motor, the motor is selected such that the desired control can be realized without causing excessive current to cause magnetic saturation. Therefore, it was assumed that L_0 and L_a are constants independent of the current value. Thus, the inter-terminal inductance of the motor L_m is determined by the combination of each inductance. From the above equations, the variation in each inductance value is a function of the rotor angle. From (4.4) and (4.7), the relationship between interlinkage magnetic flux Φ_1 and inductance value L_1 is shown in Fig. 4-4. In Fig. 4-4, L_a is assumed to be 5% the value of L_0. The resistance of each coil R_1, R_2, and R_3 does not depend on the angle, and can be considered an equal value R_0 as in

$$R_1 = R_2 = R_3 = R_0. \tag{4.10}$$

The inter-terminal resistance of the motor R_m is also the combination of each resistance, as well as L_m.

4.3 Sensorless Angle Estimation Method for BDC Motor

Angle estimation methods for the BDC motor are described in this section. As a conventional method, the counter EMF observer (CFOB) for the BDC motor is explained in section 4.3.1, and an estimation method based on impedance variation is described in section 4.3.2.

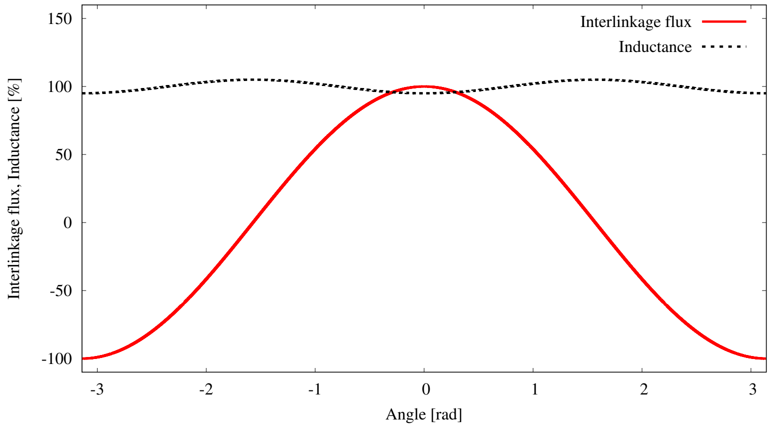

Fig. 4-4: Variation of interlinkage flux Φ_1 and inductance L_1.

4.3.1 Sensorless estimation by CFOB for BDC

From (4.1) and (4.2), the motor current is derived as follows in the frequency domain.

$$I = \frac{1}{R_m + L_m s}\left(V - K_e s\Theta\right) \tag{4.11}$$

In an actual control system, the supply voltage V is calculated by a current controller as reference voltage V^{ref}, and the motor current is measured by a current sensor as current response I^{res}. Furthermore, the motor parameters fluctuate from the nominal values due to modeling error and temperature alteration. The motor parameters are described by (4.12) and (4.13).

$$R_m = R_{mn} + \Delta R_m \tag{4.12}$$

$$L_m = L_{mn} + \Delta L_m \tag{4.13}$$

Therefore, (4.11) can be rewritten as

$$I^{res} = \frac{1}{R_{mn} + L_{mn} s}\left(V^{ref} - V_{dis}\right), \tag{4.14}$$

where

$$V_{dis} = \frac{\Delta R_m + \Delta L_m s}{R_m + L_m s} V^{ref} + \frac{R_{mn} + L_{mn} s}{R_m + L_m s} K_e s \Theta^{res}. \tag{4.15}$$

CFOB estimates the counter EMF from a voltage disturbance. Moreover, the angular velocity can be calculated by the estimated counter EMF and EMF constant, as shown in Fig. 4-5. From Fig. 4-5, the estimated angular velocity is calculated as

$$
\begin{aligned}
s\hat{\Theta}^{res} &= \frac{1}{K_{en}}\frac{g_{cfob}}{s+g_{cfob}}V_{dis} && (4.16)\\
&= \frac{g_{cfob}}{s+g_{cfob}}\Big(\frac{K_e}{K_{en}}\frac{R_{mn}+L_{mn}s}{R_m+L_m s}s\Theta^{res}\\
&\quad +\frac{1}{K_{en}}\frac{\Delta R_m+\Delta L_m s}{R_m+L_m s}V^{ref}\Big). && (4.17)
\end{aligned}
$$

Furthermore, the angle is derived as

$$\hat{\Theta}^{res} = \frac{1}{s}s\hat{\Theta}^{res}. \tag{4.18}$$

When the modeling error and parameter fluctuation are sufficiently small, the CFOB can estimate the angular velocity and angle approximately without any mechanical sensors. However, in an actual system, the modeling error and the parameter fluctuation will not become zero, and the disturbance, such as observation noise of the current sensor, also remains. Therefore, the estimated accuracy of CFOB deteriorates, especially around the zero-speed region.

4.3.2 Sensorless estimation by impedance variation

Modeling the impedance fluctuation, taking into consideration the connection state change of the brush and commutator of the BDC motor, is expressed in this section. A sensorless angle estimation method using the impedance variation is then proposed.

As mentioned in section 4.2, the inter-terminal resistance and the inter-terminal inductance of the motor depend on the connection state of each armature winding. The schematic diagram of the motor and the equivalent circuit of the armature winding in the connection state, excluding the moment when the contact point of the brush and the commutator switches, are shown in Fig. 4-6 to Fig. 4-11. From these figures, the reciprocal of the inter-terminal inductance of the motor in each connection state is

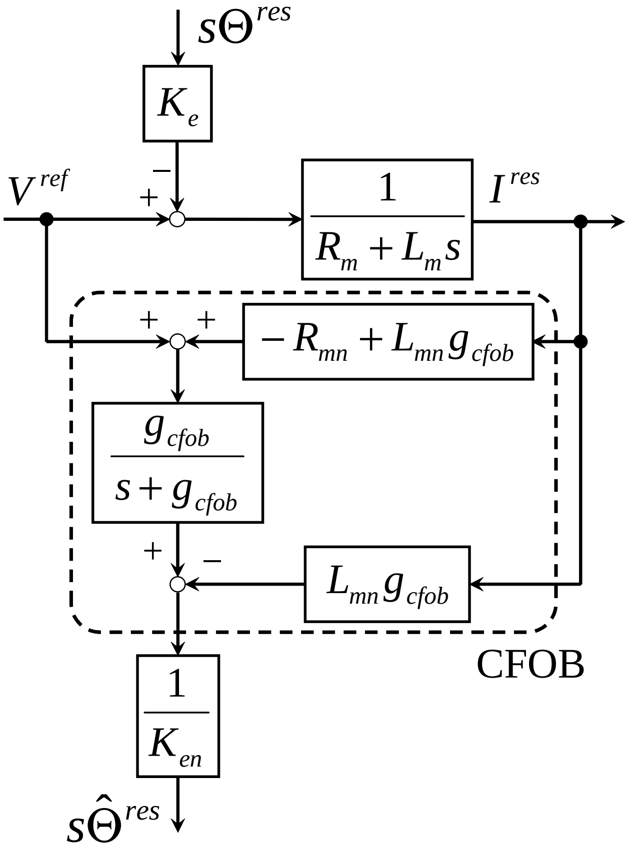

Fig. 4-5: Angular velocity estimation by CFOB.

expressed by

$$\frac{1}{L_m} = \begin{cases} \frac{1}{L_3} + \frac{1}{L_1 + L_2} \ (0 < \theta < \frac{\pi}{3} \text{ or } -\pi < \theta < -\frac{2}{3}\pi\ ) \\ \frac{1}{L_1} + \frac{1}{L_2 + L_3} \ (\frac{\pi}{3} < \theta < \frac{2}{3}\pi \text{ or } -\frac{2}{3}\pi < \theta < -\frac{\pi}{3}). \\ \frac{1}{L_2} + \frac{1}{L_3 + L_1} \ (\frac{2}{3}\pi < \theta < \pi \text{ or } -\frac{\pi}{3} < \theta < 0) \end{cases} \tag{4.19}$$

Here, focusing on the case of $\frac{\pi}{3} < \theta < \frac{2}{3}\pi$ and $-\frac{2}{3}\pi < \theta < -\frac{\pi}{3}$, which are the second row of (4.19), the inter-terminal inductance is expressed by substituting (4.7) from (4.9) as

$$L_m = \frac{2L_0^2 - L_0 L_a \cos 2\theta - L_a^2 \cos^2 2\theta}{3L_0}. \tag{4.20}$$

In the case of $0 < \theta < \frac{\pi}{3}$ and $-\pi < \theta < -\frac{2}{3}\pi$, by converting the angle to (4.21), the inter-terminal inductance becomes (4.22).

$$\theta' = \theta - \frac{2}{3}\pi \tag{4.21}$$

$$\begin{aligned} L_m &= \frac{2L_0^2 - L_0 L_a \cos 2\theta' - L_a^2 \cos^2 2\theta'}{3L_0} \\ &= \frac{2L_0^2 - L_0 L_a \cos\left\{2\left(\theta - \frac{2}{3}\pi\right)\right\} - L_a^2 \cos^2\left\{2\left(\theta - \frac{2}{3}\pi\right)\right\}}{3L_0} \end{aligned} \tag{4.22}$$

The case of $\frac{2}{3}\pi < \theta < \pi$ and $-\frac{\pi}{3} < \theta < 0$ can also be derived similarly to the above equations.

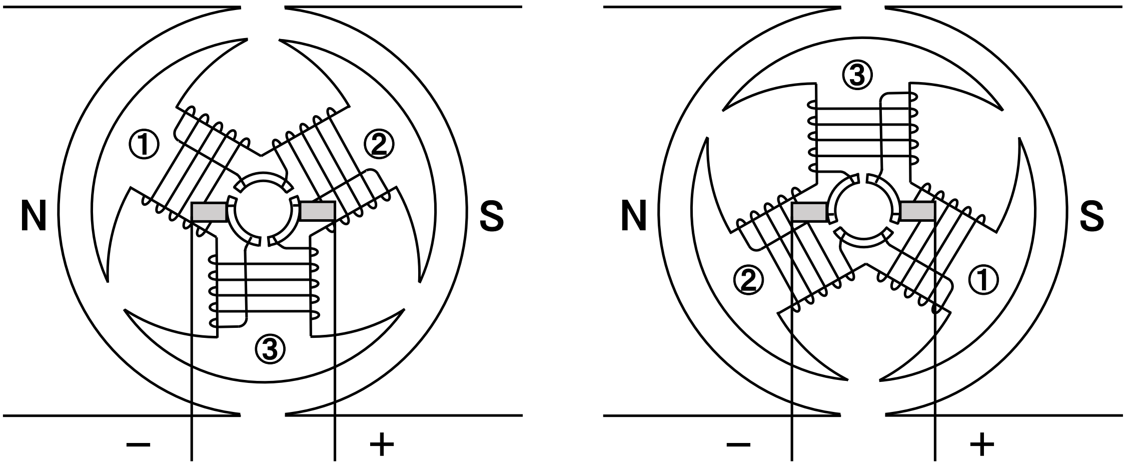

(a) $0 < \theta < \frac{\pi}{3}$ (b) $-\pi < \theta < -\frac{2}{3}\pi$

Fig. 4-6: Mechanical connection (0 to $\frac{\pi}{3}$ and $-\pi$ to $-\frac{2}{3}\pi$)

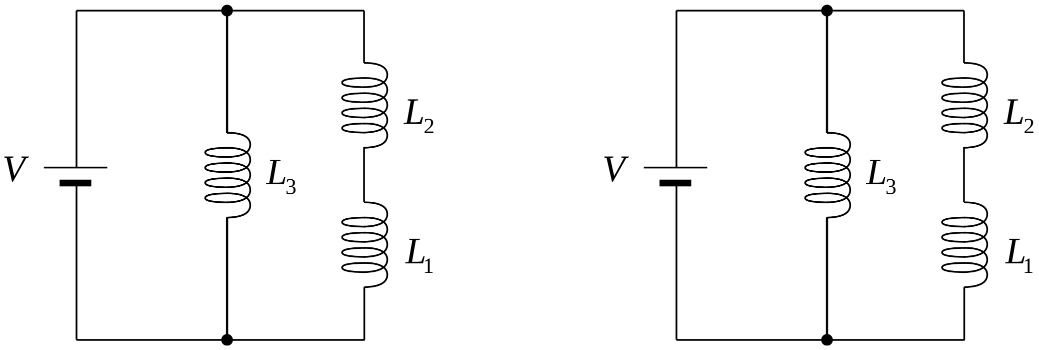

(a) $0 < \theta < \frac{\pi}{3}$ (b) $-\pi < \theta < -\frac{2}{3}\pi$

Fig. 4-7: Connection of inductance (0 to $\frac{\pi}{3}$ and $-\pi$ to $-\frac{2}{3}\pi$)

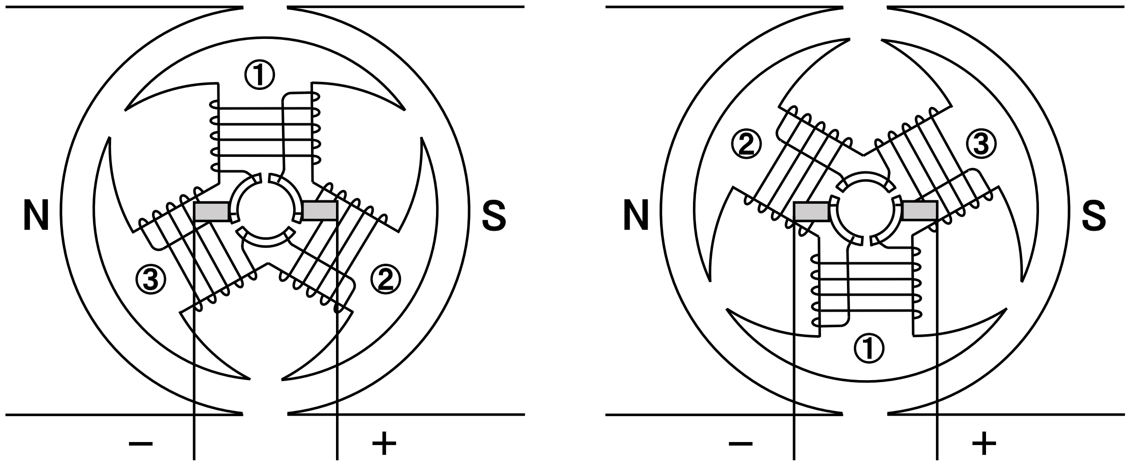

(a) $\frac{\pi}{3} < \theta < \frac{2}{3}\pi$ (b) $-\frac{2}{3}\pi < \theta < -\frac{\pi}{3}$

Fig. 4-8: Mechanical connection ($\frac{\pi}{3}$ to $\frac{2}{3}\pi$ and $-\frac{2}{3}\pi$ to $-\frac{\pi}{3}$)

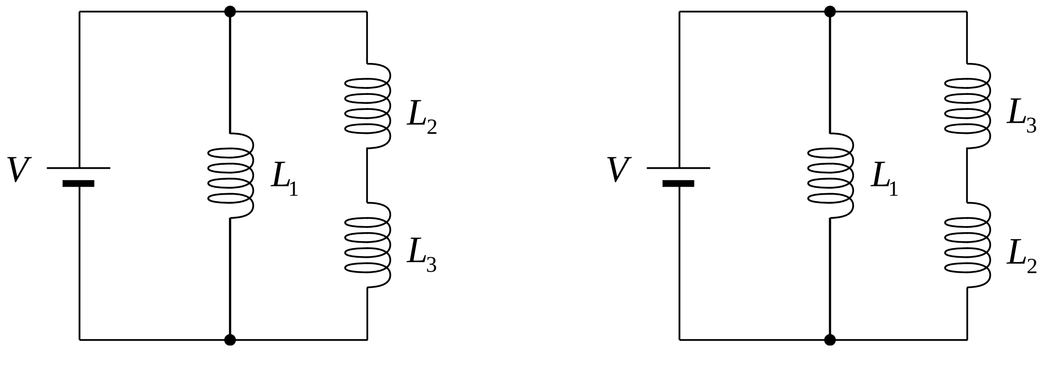

(a) $\frac{\pi}{3} < \theta < \frac{2}{3}\pi$ (b) $-\frac{2}{3}\pi < \theta < -\frac{\pi}{3}$

Fig. 4-9: Connection of inductance ($\frac{\pi}{3}$ to $\frac{2}{3}\pi$ and $-\frac{2}{3}\pi$ to $-\frac{\pi}{3}$)

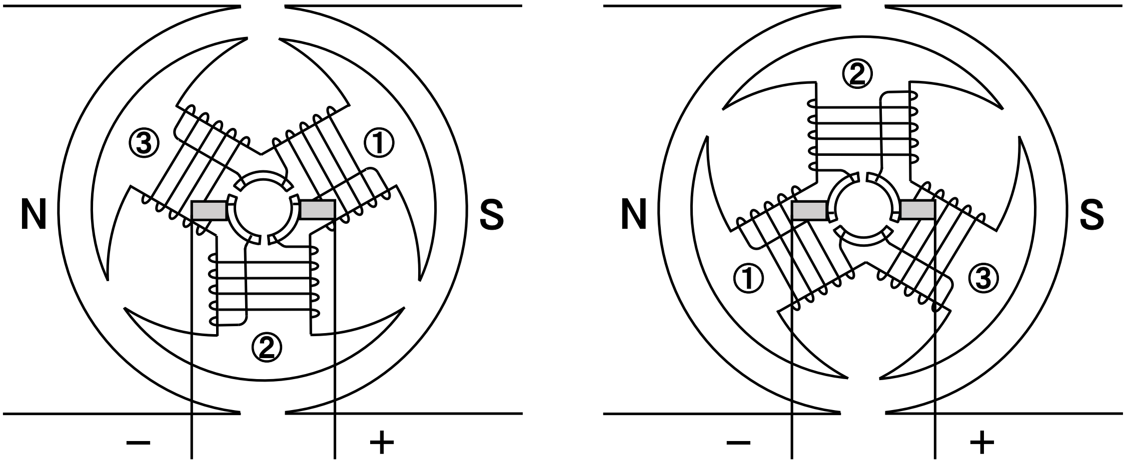

(a) $\frac{2}{3}\pi < \theta < \pi$

(b) $-\frac{\pi}{3} < \theta < 0$

Fig. 4-10: Mechanical connection ($\frac{2}{3}\pi$ to π and $-\frac{\pi}{3}$ to 0)

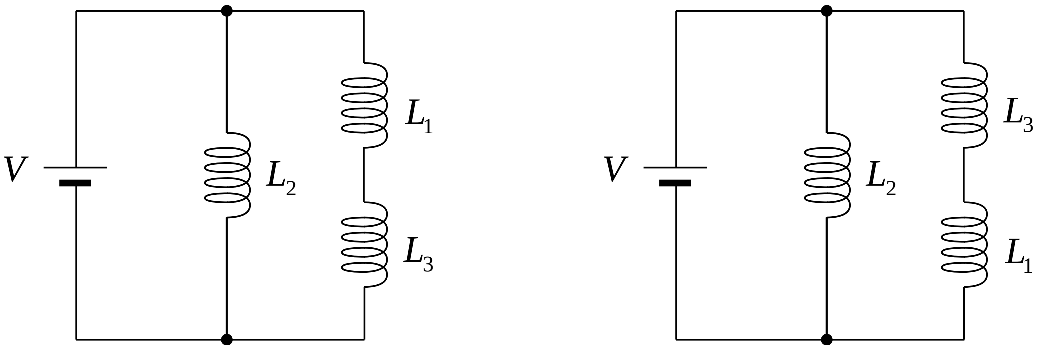

(a) $\frac{2}{3}\pi < \theta < \pi$

(b) $-\frac{\pi}{3} < \theta < 0$

Fig. 4-11: Connection of inductance ($\frac{2}{3}\pi$ to π and $-\frac{\pi}{3}$ to 0)

At the moment the point of contact between the brush and commutator switches, such as $\theta = 0, \pm\frac{\pi}{3}$, $\pm\frac{2}{3}\pi$, $\pm\pi$, the inter-terminal inductance is modeled by a different expression from the above equations because no current flows through one armature winding. For example, when $\theta = 0, \pi$, the schematic diagram and equivalent circuit of the BDC motor are shown in Fig. 4-12 and 4-13. From the figures, the reciprocal of the inter-terminal inductance is expressed by

$$\frac{1}{L_m} = \begin{cases} \dfrac{1}{L_2} + \dfrac{1}{L_3} & (\theta = 0 \text{ and } \theta = \pi) \\ \dfrac{1}{L_1} + \dfrac{1}{L_3} & (\theta = \dfrac{\pi}{3} \text{ and } \theta = -\dfrac{\pi}{3}) \\ \dfrac{1}{L_1} + \dfrac{1}{L_2} & (\theta = \dfrac{2}{3}\pi \text{ and } \theta = -\dfrac{2}{3}\pi) \end{cases} \quad . \tag{4.23}$$

By solving (4.23) and substituting (4.7) into (4.9), the inter-terminal inductance is calculated as (4.24) in every case.

$$L_m = \frac{1}{2}L_0 + \frac{1}{4}L_a \qquad \left(\theta = 0, \pm\frac{\pi}{3}, \pm\frac{2}{3}\pi, \pm\pi\right) \tag{4.24}$$

Therefore, the inter-terminal inductance of each case is derived as follows

$$L_m = \begin{cases} \dfrac{2L_0^2 - L_0 L_a \cos\left\{2\left(\theta - \frac{2}{3}\pi\right)\right\} - L_a^2 \cos^2\left\{2\left(\theta - \frac{2}{3}\pi\right)\right\}}{3L_0} & \left(0 < \theta < \dfrac{\pi}{3} \text{ or } -\pi < \theta < -\dfrac{2}{3}\pi\right) \\ \dfrac{2L_0^2 - L_0 L_a \cos 2\theta - L_a^2 \cos^2 2\theta}{3L_0} & \left(\dfrac{\pi}{3} < \theta < \dfrac{2}{3}\pi \text{ or } -\dfrac{2}{3}\pi < \theta < -\dfrac{\pi}{3}\right) \\ \dfrac{2L_0^2 - L_0 L_a \cos\left\{2\left(\theta + \frac{2}{3}\pi\right)\right\} - L_a^2 \cos^2\left\{2\left(\theta + \frac{2}{3}\pi\right)\right\}}{3L_0} & \left(\dfrac{2}{3}\pi < \theta < \pi \text{ or } -\dfrac{\pi}{3} < \theta < 0\right) \\ \dfrac{1}{2}L_0 + \dfrac{1}{4}L_a & \left(\theta = 0, \pm\dfrac{\pi}{3}, \pm\dfrac{2}{3}, \pm\pi\right) \end{cases} \tag{4.25}$$

To consider the inter-terminal resistance, as the resistance value of each armature winding is same regardless of the angle from (4.10), the inter-terminal resistance, excluding the moment of switching

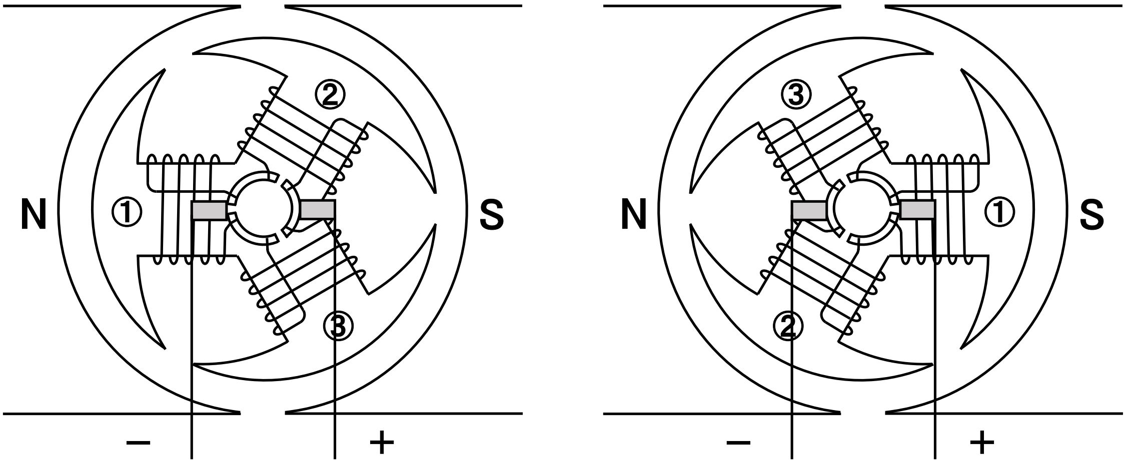

(a) $\theta = 0$

(b) $\theta = \pi$

Fig. 4-12: Mechanical connection ($\theta = 0$ and $\theta = \pi$)

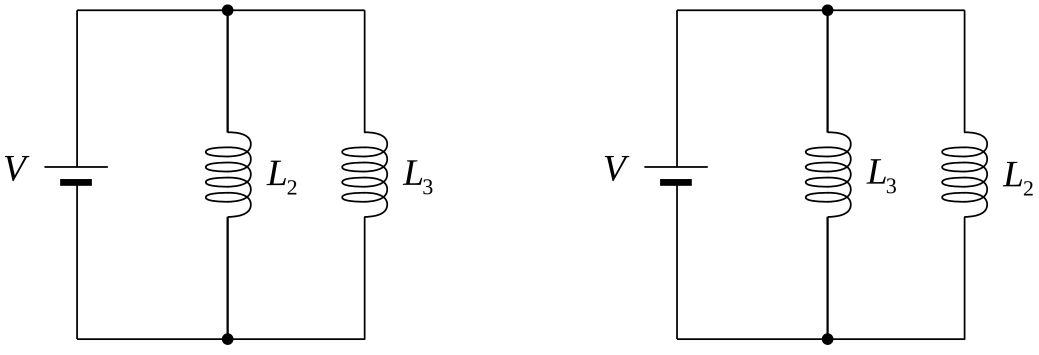

(a) $\theta = 0$

(b) $\theta = \pi$

Fig. 4-13: Connection of inductance ($\theta = 0$ and $\theta = \pi$)

contact between the brush and commutator, is expressed by

$$\begin{aligned}\frac{1}{R_m} &= \frac{1}{R_0} + \frac{1}{R_0 + R_0} \\ R_m &= \frac{2}{3}R_0\end{aligned} \qquad \left(\theta \neq 0, \pm\frac{\pi}{3}, \pm\frac{2}{3}\pi, \pm\pi\right). \tag{4.26}$$

The inter-terminal resistance at the moment of switching contact between the brush and the commutator is expressed by

$$\begin{aligned}\frac{1}{R_m} &= \frac{1}{R_0} + \frac{1}{R_0} \\ R_m &= \frac{1}{2}R_0\end{aligned} \qquad \left(\theta = 0, \pm\frac{\pi}{3}, \pm\frac{2}{3}\pi, \pm\pi\right). \tag{4.27}$$

As a result, in the BDC motor, the angle dependence of the inter-terminal impedance variation combining inter-terminal inductance and inter-terminal resistance can be modeled.

In this research, the inter-terminal impedance is measured by applying a high-frequency voltage and detecting the current response. In order to analyze the response of a high-frequency band, the current flowing through the BDC motor is converted to

$$i = i_L + i_H, \tag{4.28}$$

where subscripts L and H denote the low and high-frequency components, respectively. The signal related to the motion control of the motor is treated as the low-frequency band. The signal related to the voltage applied for the impedance measurement is treated as the high-frequency band. Because of the mechanical time constant of the motor, the effect of the high-frequency current component will not appear in the motion control. By substituting (4.28) into (4.1), (4.29) is derived as

$$v = R_m i_H + R_m i_L + L_m \frac{di_H}{dt} + L_m \frac{di_L}{dt} + K_e \dot{\theta}. \tag{4.29}$$

In (4.29), because the counter EMF depends on the angular velocity of the motor, it can be regarded as a component in the low-frequency band. Thus, by decomposing the counter EMF into low-frequency-band components and high-frequency-band components, the following equations are obtained.

$$v = v_L + v_H \tag{4.30}$$

$$v_L = R_m i_L + L_m \frac{di_L}{dt} + K_e \dot{\theta} \tag{4.31}$$

$$v_H = R_m i_H + L_m \frac{di_H}{dt} \tag{4.32}$$

As mentioned before, v_H denotes the high-frequency voltage used for impedance measurement. Therefore, the injected voltage signal v_{inj} is expressed by

$$v_{inj} = v_H = v_A \sin(\omega t), \tag{4.33}$$

where, t, v_A and ω denote the time, amplitude and angular frequency of the injected voltage signal, respectively. When v_{inj} is expressed by (4.33), the current response caused by the injected voltage i_H is derived as

$$i_H = i_A \sin(\omega t + \phi), \tag{4.34}$$

where i_A and ϕ represent the amplitude of the current response i_H and the phase difference between the voltage and the current, respectively. From (4.32), (4.33) and, (4.34), the relation between each amplitude is derived as

$$v_A = i_A \sqrt{{R_m}^2 + (\omega L_m)^2}, \tag{4.35}$$

$$= i_A |Z_m|. \tag{4.36}$$

Z_m is the impedance of the motor. This research does not consider a floating capacitance of the motor. Therefore, the phase difference between the voltage and the current is represented as

$$\phi = \tan^{-1} \frac{\omega L_m}{R_m}, \tag{4.37}$$

and by solving (4.35), an absolute value of impedance $|Z_m|$ is derived as

$$|Z_m| = \frac{v_A}{i_A}. \tag{4.38}$$

This equation exhibits the inter-terminal impedance of the BDC motor calculated by high-frequency signal injection. Here, the amplitude of the injected voltage v_A is a known value that has been set by the

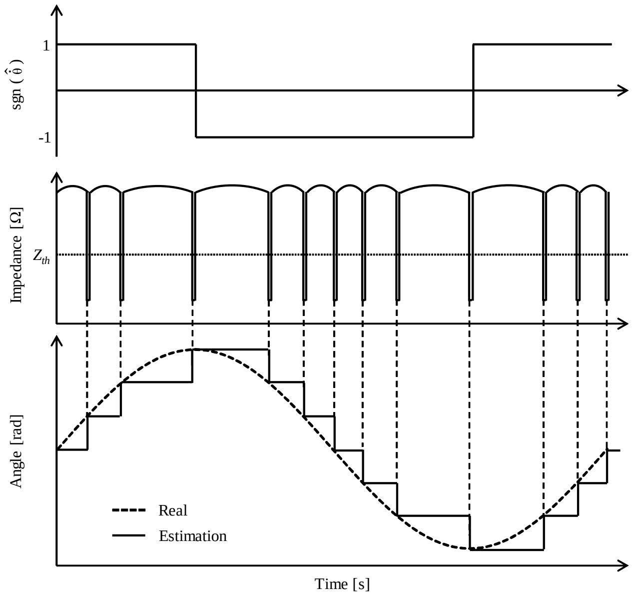

Fig. 4-14: Conceptual diagram of estimation algorithm.

user, and the amplitude of the current response i_A can be calculated from the current values measured by the current sensor and synchronous detection. For synchronous detection, this research uses the discrete Fourier transform (DFT). The impedance measurement becomes possible without influence from the frequency related to motion control because of DFT.

To estimate the angle from the inter-terminal impedance, the pulse variations of inter-terminal impedance are modeled by (4.26), (4.27), and (4.25). From the model, the pulse variation of the impedance has periodically occurred. Therefore, by setting the impedance threshold Z_{th} in advance, a virtual comparator is arranged. The comparator detects the inter-terminal impedance-fluctuation pulse waveform; then, the estimated angle is updated. However, this method cannot detect the direction of rotation. In order to solve this problem, this research incorporates an angular velocity estimation value from CFOB into the signum function and performs rotational direction detection. The angle estimation method using the proposed method is expressed by

$$\hat{\theta}_{new} = \begin{cases} \hat{\theta}_{old} & \text{(when undetect the pulse)}, \\ \hat{\theta}_{old} + \mathrm{sgn}\left(\hat{\dot{\theta}}\right)\dfrac{\pi}{3} & \text{(when detect the pulse)}, \end{cases} \tag{4.39}$$

where the subscripts new and old are the values after and before the update, respectively. The concept of this method is shown in Fig. 4-14. Hence, this algorithm can emulate the low-resolution encoder

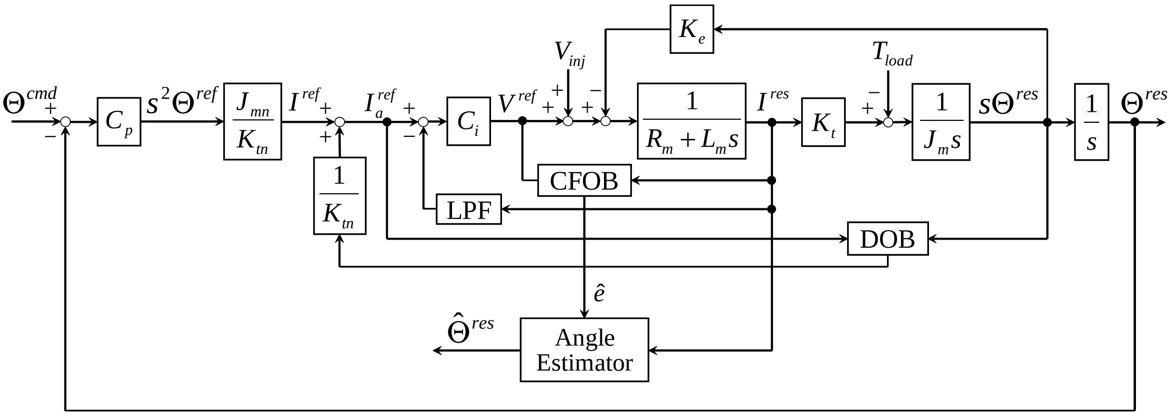

Fig. 4-15: Block diagram of proposed sensorless angle estimation.

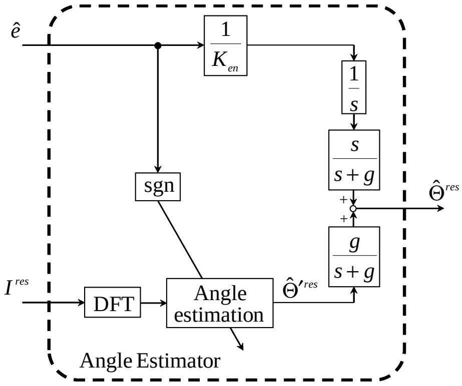

Fig. 4-16: Angle estimator for BDC motor.

in sensorless systems. Therefore, the proposed method can be combined with the method described in Chapter 3, and the estimated angle is derived as

$$\hat{\Theta}^{res} = \frac{g}{s+g}\hat{\Theta}'^{res} + \frac{s}{s+g}\frac{1}{s}s\hat{\Theta}^{res}. \tag{4.40}$$

Here, g denotes a cutoff frequency of the low- and high-pass filters, and $\hat{\Theta}'^{res}$ is an estimated value based on the impedance detection. As a result, a block diagram incorporating the sensorless angle estimation method proposed in this chapter into the angle control system is shown in Fig. 4-15 and 4-16. Here, C_p and C_i are the proportional-derivative position controller and the proportional-integral current controller

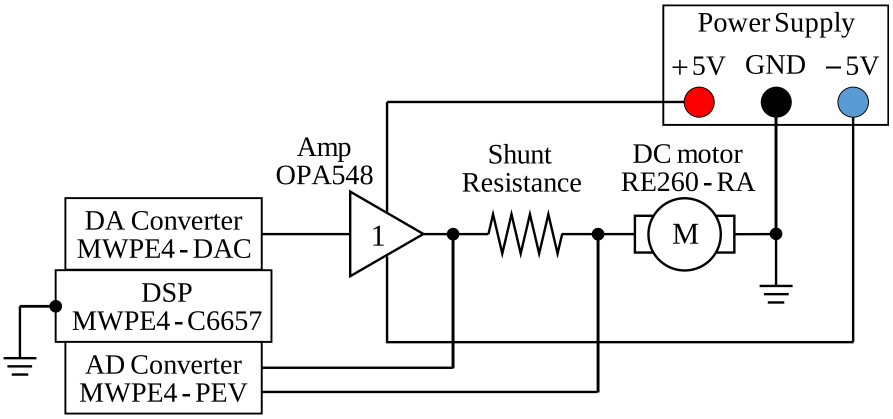

Fig. 4-17: Schematic diagram of experimental setup.

expressed by (4.41) and (4.42), respectively.

$$C_p = K_p + K_v s \tag{4.41}$$

$$C_i = K_{pi} + K_{ii}\frac{1}{s} \tag{4.42}$$

To reduce the effect on the current controller caused by the high-frequency signal injection, the low-pass filter is inserted into the current loop.

4.4 Experiments

This section describes the confirmation of the validity of the proposed estimation method. First, model verification experiments are carried out to verify the validity of the angle-dependent impedance model. After that, the state of pulse detection while increasing the angular velocity is verified, and the range of angular velocity to which this method can be applied is checked. Finally, the proposed estimation method is incorporated into the angle control system and the estimation accuracy is verified.

4.4.1 Outline of experiments

A schematic diagram of the experiment is shown in Fig. 4-17, and an actual experimental setup is shown in Fig. 4-18. In this research, a 3-slot BDC motor “RE260-RA” made by MABUCHI MOTOR CO., LTD. was utilized. A 500-pulse rotary encoder “MES-6-500P” made by Microtech Laboratory Inc. was used for measuring the real angle. For calculation processing and the input/output of the control

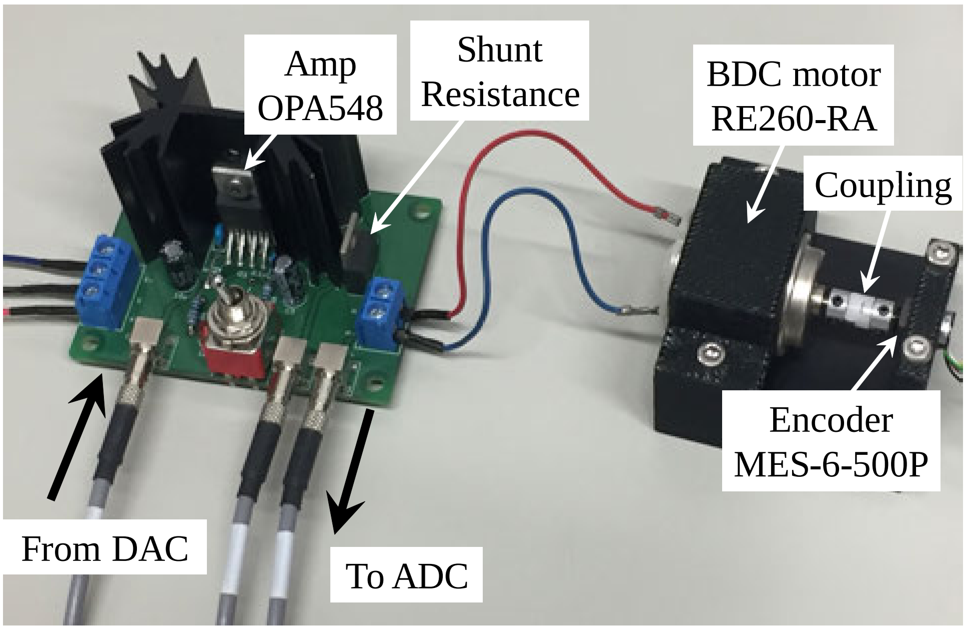

Fig. 4-18: Actual experimental setup.

system, “PE-Expert4” made by Myway Plus Corporation was utilized. In the PE-Expert4, the operation clock of the DSP board (MWPE4-C6657) was 1.25 GHz, the resolution of the AD converter in the PEV board (MWPE4-PEV) was 14 bits, and the resolution and range of the DA converter in the DA board (MWPE4-DAC) were 16 bits and ± 10 V, respectively. The sampling time of the current controller and position controller were 10 μs and 100 μs, respectively. The high-frequency voltage signal expressed by (4.43) was injected to the BDC motor.

$$v_{inj} = 2.0 \sin(2000.0\pi t) \tag{4.43}$$

Equation (4.43) indicates that the amplitude and frequency of the injected signal are 2.0 V and 1 kHz, respectively. By setting the amplitude to 2.0 V with respect to the constant operating voltage of the motor of 3.0 V, sufficiently high-frequency current response value acquisition is realized. The frequency of the applied voltage should not influence the motor drive, and high frequencies are desired in order to reduce audible acoustic noise. However, DFT needs to be performed with a sufficient number of samples. Based on the above viewpoints, a 1 kHz was adopted in this research. The window size of DFT was set to 1 ms to analyze the response of 1 kHz, and the calculation was performed on 100 sample data every 10 μs. The parameters utilized in this chapter are shown in Table 4.1.

Table 4.1: Common parameters utilized in experiments.

Symbol	Meanings of the parameter	Value
J_{mn}	Nominal moment of inertia	$15.95\times10^{-7}\mathrm{kg}\cdot\mathrm{m}^2$
K_{tn}	Nominal torque constant	1.98 mNm/A
K_{en}	Nominal counter EMF constant	2.05 mV/(rad/s)
R_{mn}	Nominal resistance	1.6 Ω
L_{0n}	Nominal inductance	0.34 mH
L_{an}	Nominal inductance	0.03 mH
g_{cfob}	Cutoff frequency of CFOB	10 rad/s
g	Cutoff frequency of LPF and HPF	2 π rad/s
Z_{th}	Threshold of impedance	2.9 Ω
K_{ii}	Integral gain of C_i	1000.0
K_{pi}	Proportional gain of C_i	2.0
$-$	Cutoff frequency of LPF(I^{res})	300 rad/s
K_p	Proportional gain	3600 $1/s^2$
K_v	Derivative gain	120 $1/s$

4.4.2 Experiment for model validation

The validity of the impedance model shown in (4.26), (4.27), and (4.25) is verified in this section. The impedance value was measured by the method using DFT described in section 4.3.2. The rotational velocity in this experiment was set to an extremely low value of 3 rpm in order to remove the effect of counter EMF as much as possible. A comparison result of the modeled inter-terminal impedance and the measured inter-terminal impedance is shown in Fig. 4-19, where the red solid line denotes the measured inter-terminal impedance and the black dashed line denotes the impedance calculated by the model. From the figure, the pulse variation of impedance is accurately matched. Therefore, the validity of the model is confirmed.

4.4.3 Experiment for applicability range confirmation

In the proposed estimation method, due to the mechanism of detecting impedance pulses by DFT, restrictions exist in the applicable angular velocity ranges. The restriction depends on the structural elements of the motor, the contact area between the brush and the commutator, and the parameters of the proposed method such as the frequency of the applied voltage and the sampling frequency during DFT operation. In this section, the range of angular velocity to which the proposed estimation method

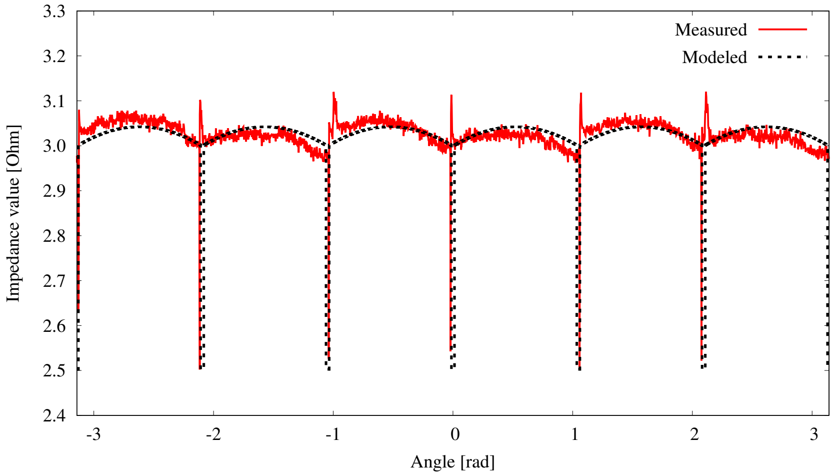

Fig. 4-19: Experimental result of impedance measurement.

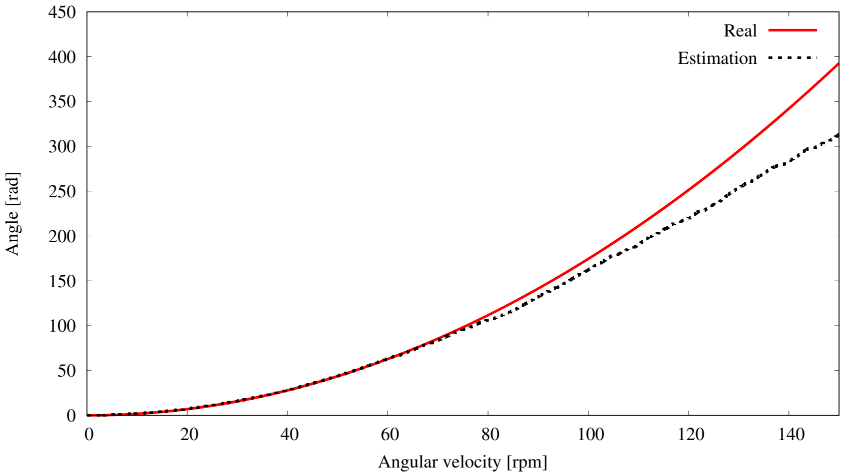

Fig. 4-20: Experimental result of angular velocity limit verification.

can be applied was confirmed by experiment. In the confirmation experiment, the pulse variation of the impedance was detected while rotating the motor at a constant acceleration in a fixed direction. For each detection, $\frac{\pi}{3}$ was added to the estimated angle and compared with the actual angle measured by the encoder. The experimental result is shown in Fig. 4-20. From Fig. 4-20, pulse skipping occurs from around 70 rpm. The range of applicable angular velocity can be expanded by raising the frequency of the applied voltage, and raising the sampling frequency of the computing unit. However, the aim of the proposed estimation method in this research is to estimate the angular velocity at low speeds.. Therefore, the experimental result indicates that the currently applicable range is sufficient. Outside of the angular velocity range, to combine with conventional methods such as counter EMF, the angular velocity can be estimated in a wide range by combining with conventional methods such as counter EMF. The range that can be estimated will be widened.

4.4.4 Experiment for sensorless angle estimation

In this section, the validity of the proposed estimation method is confirmed by experimental results. The threshold value of the impedance used in the proposed estimation method is 2.9 Ω, according to the model and nominal value, and the angle command of the experiment was a 0.1-Hz sinusoidal wave. In addition, the cutoff frequency of CFOB was set to 10 rad/s because the objective is only a positive/negative judgment, and the influence of noise should be eliminated as much as possible. The experimental results of the conventional method (CFOB) and the proposed method are shown in Fig. 4-21, Fig. 4-22, and Fig. 4-23. In these figures, the red solid line, black dashed line, blue dash-dotted line, and green dotted line denote the angle command, actual angle response, estimated angle response, and error between the actual and estimated values, respectively. According to the conventional method shown in Fig. 4-21, a drift phenomenon occurred, and an accurate angle estimation could not be achieved. Therefore, the estimation error increased with the passage of time. In the proposed method shown in Fig. 4-22, the estimation error was within 0.7 rad at the maximum. This error is caused by the principle of the proposed method of detecting the switching between the brush and the commutator based on impedance variation. The behavior of the estimation error varies depending on the initial angle, and it can be a value such as $0 \sim \frac{\pi}{3}$rad, $\frac{\pi}{3} \sim 0$rad, or $-\frac{\pi}{6} \sim \frac{\pi}{6}$rad. Therefore, depending on the condition, an estimation error of 1 rad occurs. However, no phenomena, such as an increase in estimation error due to the passage of time, occur. Furthermore, it was confirmed that a more accurate angle estimation could be achieved compared with the conventional method, because the conventional method calculates the angle after estimating the angular velocity, whereas the proposed method can directly estimate the angle. The estimated angle determined by combining the proposed method in this chapter and the method in chapter 3 is shown in Fig. 4-23. From Fig. 4-23, accurate angle information can be obtained by the proposed methods.

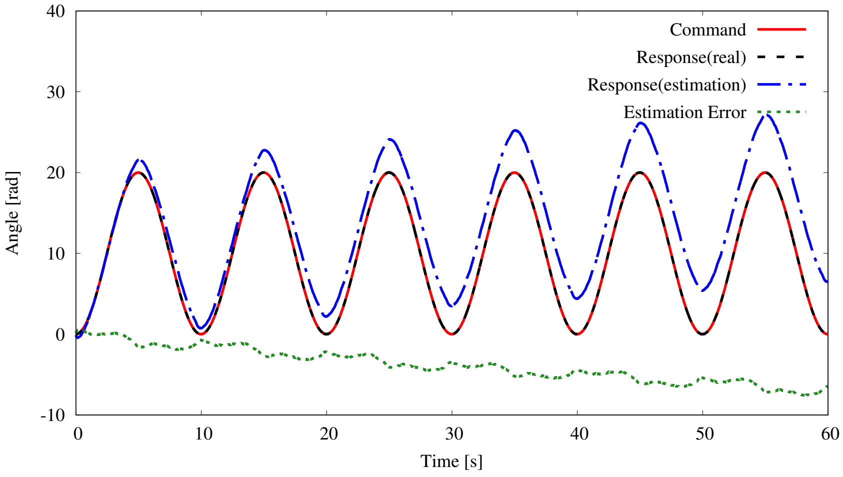

Fig. 4-21: Experimental result of conventional angle estimation.

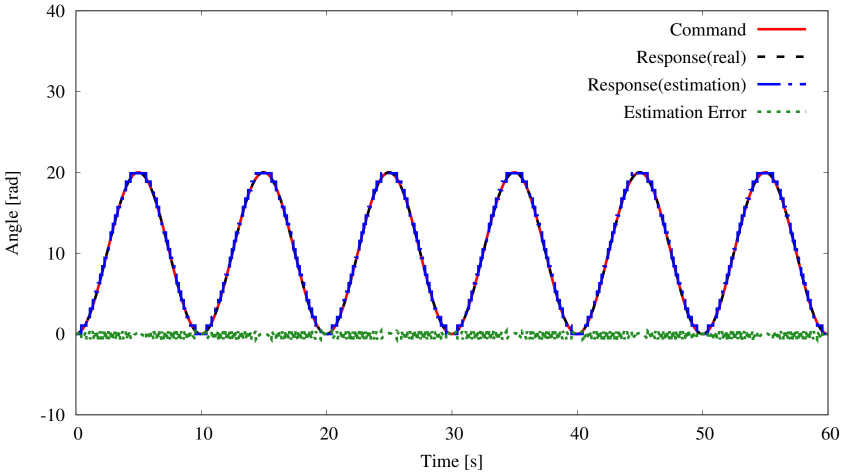

Fig. 4-22: Experimental result of proposed angle estimation (only impedance detection).

4.5 Summary

In this chapter, a sensorless angle estimation method for the BDC motor using impedance variation due to contact switching was proposed. The validity and usefulness of the proposed impedance model

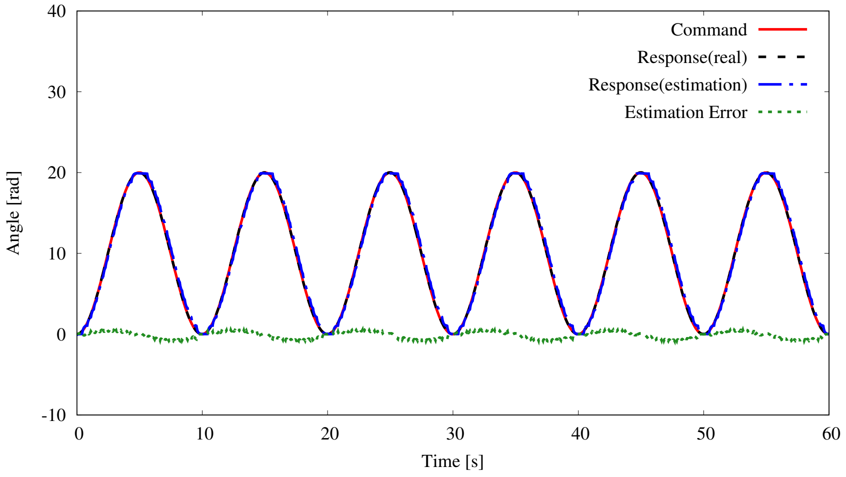

Fig. 4-23: Experimental result of proposed angle estimation.

and proposed estimation method were shown by the experiment. The experimental results confirmed that the proposed method can estimate the angle more accurately than the conventional method using counter EMF, without causing a drift phenomenon.

Chapter 5

Conclusions

Electrical actuators are widely used in various applications, such as vehicles, home appliances, robots, fans, and drones. Furthermore, many applications that are necessary to control the position and velocity of actuators are becoming increasingly popular. These controls are achieved by using high-resolution position sensors. However, high-resolution sensors increase the maintenance requirements, failure rate, size of systems, and cost. They require special machine construction, such as a second shaft end to couple the sensor. In order to solve these problems, interest in precise control with sensorless or low-resolution encoders is increasing. The purpose of this research is to achieve precise control using the sensorless or low-resolution encoder for the rotary electric actuator.

Chapter 1 summarized the background and previous studies about sensorless and low-resolution techniques. Chapter 2 described the fundamental technology of motion control based on robust acceleration control with DOB. Angle control and torque control based on the robust acceleration control were explained. Furthermore, as a space-restricted application, the motion control of a two-link manipulator equipped with a biarticular muscle mechanism considered for use in humanoid machines was outlined. Chapter 3 described the angle estimation method for the BLDC motor. The model of the three-phase BLDC motor was explained. The usage of the Hall sensor as a low-resolution angle sensor was described, and then the method to extend CFOB to the BLDC motor was explained. By combining these methods, a method using the digital Hall sensor and counter EMF was proposed. The sensorless angle estimation method for the BDC motor was explained in chapter 4. CFOB for the BDC motor was also described. Furthermore, the angle dependence of the inter-terminal impedance variation combining inter-terminal inductance and inter-terminal resistance was modeled. The proposed method focused on pulse variation due to contact switching. The impedance was measured by high-frequency signal injection and synchronous detection. The proposed method detects the inter-terminal impedance-variation pulse waveform and then adds or subtracts it to estimate the angle. Additionally, the proposed method incorporates the angular velocity estimation value by CFOB into the signum function and performs rotational direction detection.

In summary, the proposed algorithm for the BLDC motor using the Hall sensor and counter EMF could achieve high-performance angle estimation and control in comparison with the counter EMF based method and the method only using the Hall sensor. Robustness against modeling error was also confirmed by simulations and experiments. The proposed algorithm for the BDC motor using the impedance variation could estimate the angle without causing a drift phenomenon, and was more accurate than the conventional method using counter EMF.

References

[1] V. Duchaine, B. M. St.-Onge, D. Gao, and C. Gosselin, “Stable and intuitive control of an intelligent assist device”, *IEEE Trans. Haptics*, Vol. 5, No. 2, pp. 148–159, Apr. 2012.

[2] S. Ueki, H. Kawasaki, S. Ito, Y. Nishimoto, M. Abe, T. Aoki, Y. Ishigure, T Ojika, and T. Mouri, “Development of a hand-assist robot with multi-degrees-of-freedom for rehabilitation therapy”, *IEEE/ASME Trans. Mechatronics*, Vol. 17, No. 1, pp. 136–146, Feb. 2012.

[3] K. Kiguchi and Y. Hayashi, “An emg-based control for an upper-limb power-assist exoskeleton robot”, *IEEE Trans. Systems, Man, and Cybernetics PART B: Cybernetics*, Vol. 42, No. 4, pp. 1064–1071, Aug. 2012.

[4] T. Shibata and T. Murakami, “Power-assist control of pushing task by repulsive compliance control in electric wheelchair”, *IEEE Trans. Ind. Electron.*, Vol. 59, No. 1, pp. 511–520, Jan. 2012.

[5] S. Oh, K. Kong, and Y. Hori, “Design and analysis of force-sensor-less power-assist control”, *IEEE Trans. Ind. Electron.*, Vol. 61, No. 2, pp. 985–993, Feb. 2014.

[6] J. Huang, W. Huo, W. Xu, S. Mohammed, and Y. Amirat, “Mcontrol of upper-limb power-assist exoskeleton using a human-robot interface based on motion intention recognition”, *IEEE Trans. Autom. Sci. Eng.*, Vol. 12, No. 4, pp. 1257–1270, Oct. 2015.

[7] S. M. M. Rahman and R. Ikeura, “Weight-prediction-based predictive optimal position and force controls of a power assist robotic system for object manipulation”, *IEEE Trans. Autom. Sci. Eng.*, Vol. 63, No. 9, pp. 5964–5975, Sep. 2016.

[8] I. Boldea, “Control issues in adjustable speed drives”, *IEEE Trans. Ind. Electron. Mag.*, Vol. 2, No. 3, pp. 32–50, Sep. 2008.

[9] J. W. Finch and D. Giaouris, “Controlled ac electrical drives”, *IEEE Trans. Ind. Electron.*, Vol. 55, No. 2, pp. 481–491, Feb. 2008.

[10] K. Kondo and S. Doki, “Position estimation system for pmsm position sensorless vector control operable up to inverter overmodulation range”, *IEEJ Trans. IA*, Vol. 136, No. 11, pp. 829–836, Nov. 2016.

[11] H. Zoubek and M. Pacas, “Encoderless identification of two-mass-systems utilizing an extended speed adaptive observer structure”, *IEEE Trans. Ind. Electron.*, Vol. 64, No. 1, pp. 595–604, Jan. 2017.

[12] F. Wang, Z. Zhang, S. A. Davari, R. Fotouhi, D. Arab Khaburi, J. Rodrguez, and R. Kennel, “An encoderless predictive torque control for an induction machine with a revised prediction model and efosmo”, *IEEE Trans. Ind. Electron.*, Vol. 61, No. 12, pp. 6635–6644, Dec. 2014.

[13] S. Murakami, T. Shiota, M. Ohto, K. Ide, and M. Hisatsune, “Encoderless servo drive with adequately designed ipmsm for pulse-voltage-injection-based position detection”, *IEEE Trans. Ind. Appl.*, Vol. 48, No. 6, pp. 1922–1930, Nov. 2012.

[14] T. Takeshita, M. Ichikawa, J. Lee, and N. Matsui, “Back emf estimation-based sensorless salient-pole brushless dc motor drives”, *IEEJ Trans. IA*, Vol. 117, No. 1, pp. 98–104, Jan. 1997.

[15] C. Zhiqian, M. Tomita, and S. Okuma, “An extended electromotive force model for sensorless control of interior permanent-magnet synchronous motors”, *IEEE Trans. Ind. Electron.*, Vol. 50, No. 2, pp. 288–295, Apr. 2003.

[16] S. C. Yang and Y. L. Hsu, “Full speed region sensorless drive of permanent-magnet machine combining saliency-based and back-emf-based drive”, *IEEE Trans. Ind. Electron.*, Vol. 64, No. 2, pp. 1092–1101, Feb. 2017.

[17] S. C. Yang and G. R. Chen, “High-speed position-sensorless drive of permanent-magnet machine using discrete-time emf estimation”, *IEEE Trans. Autom. Sci. Eng.*, Vol. 64, No. 6, pp. 4444–4453, Jun. 2017.

[18] P. M. Johnson, K. Bai, and X. Ding, “Back-emf-based sensorless control using the hijacker algorithm for full speed range of the motor drive in electrified automobile systems”, *IEEE Trans. Transport. Electrific.*, Vol. 1, No. 2, pp. 126–137, Aug. 2015.

[19] R. Leidhold, “Position sensorless control of pm synchronous motors based on zero-sequence carrier injection”, *IEEE Trans. Ind. Electron.*, Vol. 58, No. 12, pp. 5371–5379, Dec. 2011.

[20] S. Kim, J. Ha, and S. Sul, “Pwm switching frequency signal injection sensorless method in ipmsm”, *IEEE Trans. Ind. Appl.*, Vol. 48, No. 5, pp. 1576–1587, Sep. 2012.

[21] R. Hosooka, S. Shinnaka, and N. Nakamura, “New sensorless vector control of pmsm by discrete-time voltage injection of pwm carrier frequency”, *IEEJ Trans. IA*, Vol. 136, No. 11, pp. 837–850, Nov. 2016.

[22] G. Xie, K. Lu, S. K. Dwivedi, J. R. Rosholm, and F. Blaabjerg, “Minimum-voltage vector injection method for sensorless control of pmsm for low-speed operations”, *IEEE Trans. Power Electron.*, Vol. 31, No. 2, pp. 1785–1794, Feb. 2016.

[23] Y. Iwaji, R. Takahata, T. Suzuki, and S. Aoyagi, “Position sensorless control method at zero-speed region for permanent magnet synchronous motors using the neutral point voltage of stator windings”, *IEEE Trans. Ind. Appl.*, Vol. 52, No. 5, pp. 4020–4028, Sep. 2016.

[24] S. C. Yang and Y. L. Hsu, “Full speed region sensorless drive of permanent-magnet machine combining saliency-based and back-emf-based drive”, *IEEE Trans. Ind. Electron.*, Vol. 64, No. 2, pp. 1092–1101, Feb. 2017.

[25] R. Yasumoto and S. Kondo, “Speed control of pm motor using method of combining low-resolution encoder with estimation position error compensation”, In *Japan Industry Appl. Soc. Technical Committee on Semiconductor Power Converter*, pp. 27–32, Nov. 2006.

[26] L. Kovudhikulrungsri and T. Koseki, “Precise speed estimation from a low-resolution encoder by dual-sampling-rate observer”, *IEEE/ASME Trans. Mechatronics*, Vol. 11, No. 6, pp. 661–670, Dec. 2006.

[27] S. Kim, C. Choi, K. Lee, and W. Lee, “An improved rotor position estimation with vector-tracking observer in pmsm drives with low-resolution hall-effect sensors”, *IEEE Trans. Ind. Electron.*, Vol. 58, No. 9, pp. 4078–4086, Sep. 2011.

[28] Y. Liu, J. Zhao, M. Xia, and H. Luo, “Model reference adaptive control-based speed control of brushless dc motors with low-resolution hall-effect sensors”, *IEEE Trans. Ind. Electron.*, Vol. 29, No. 3, pp. 1514–1522, Mar. 2014.

[29] Y. Kambara, S. Uozumi, T. Nozaki, and K. Ohnishi, “Position-sensorless motion control of dc motor”, *IEEJ Trans. IA*, Vol. 135, No. 3, pp. 205–211, Mar. 2015.

[30] Y. Kambara, S. Uozumi, and K. Ohnishi, “Disturbance suppression method for position-sensorless motion control of dc brushed motor”, In *Mechatronics (ICM), 2015 IEEE International Conference on*, pp. 194–199, Mar. 2015.

[31] P. Radcliffe and D. Kumar, “Sensorless speed measurement for brushed dc motors”, *Power Electronics, IET*, Vol. 8, No. 11, pp. 2223–2228, Nov. 2015.

[32] C. T. Chi and S. A. Yin, “Speed measurement of a general dc brushed motor based on sensorless method”, In *Proc. Int. Conf. IPEC*, pp. 332–337, Dec. 2012.

[33] R. M. Ramli, N. Mikami, and H. Takahashi, “Adaptive filters for rotational speed estimation of a sensorless dc motor with brushes”, In *Proc. 2010 10th Int. Conf. ISSPA*, pp. 562–565, May 2010.

[34] E. Vazquez-Sanchez, J. Gomez-Gil, J. C. Gamazo-Real, and J. F. DiezHiguera, “A new method for sensorless estimation of the speed and position in brushed dc motors using support vector machines”, *IEEE Trans. Ind. Electron.*, Vol. 59, No. 3, pp. 1397–1408, Mar. 2012.

[35] J. M. Knezevic, “Low-cost low-resolution sensorless positioning of dc motor drives for vehicle auxiliary applications”, *IEEE Trans. Veh. Technol*, Vol. 62, No. 9, pp. 4328–4335, Nov. 2013.

[36] K. Ohnishi, M. Shibata, and T. Murakami, “Motion control for advanced mechatronics”, *IEEE/ASME Trans. Mechatronics*, Vol. 1, No. 1, pp. 56–67, Mar. 1996.

[37] T. Murakami, F. Yu, and K. Ohnishi, “Torque sensorless control in multidegree-of-freedom manipulator”, *IEEE Trans. Ind. Electron.*, Vol. 40, No. 2, pp. 259–265, Apr. 1993.

[38] C. Mitsantisuk, K. Ohishi, and S. Katsura, “Estimation of action/reaction forces for the bilateral control using kalman filter”, *IEEE Trans. Ind. Electron.*, Vol. 59, No. 11, pp. 4383–4393, Jun. 2012.

[39] N. Hogan, “Adaptive control of mechanical impedance by coactivation of antagonist muscles”, *IEEE Trans. Automat. Contr.*, Vol. 29, No. 8, pp. 681–690, Aug. 1984.

[40] H. Fukusho, T. Koseki, and T. Sugimoto, “Control of a straight line motion for a two-link robot arm using coordinate transform of bi-articular simultaneous drive”, In *2010 11th IEEE International Workshop on Advanced Motion Control (AMC)*, pp. 786–791, Mar. 2010.

[41] H. Lee, H. I. Krebs, and N. Hogan, “Multivariable dynamic ankle mechanical impedance with relaxed muscles”, *IEEE Trans. Neural Syst. Rehabil. Eng.*, Vol. 22, No. 6, pp. 1104–1114, Nov. 2014.

[42] N. A. Hakansson and M. L. Hull, “Influence of pedaling rate on muscle mechanical energy in low power recumbent pedaling using forward dynamic simulations”, *IEEE Trans. Neural Syst. Rehabil. Eng.*, Vol. 15, No. 4, pp. 509–516, Dec. 2007.

List of Achievements

Journals (As a first author)

[1] Yuki Saito, Kazuma Nakai, Hiromu Sekiguchi, Satoshi Fukushima, Takahiro Nozaki, and Kouhei Ohnishi, "Sensorless Angle Estimation Method for Brushed DC Motor using Impedance Variation by Contact Switching," *IEEJ Transactions on Industry Applications*, Vol. 137-D, No. 11, pp. 827–836, Nov. 2017. (in Japanese)

[2] Yuki Saito, Wataru Motooka, Takahiro Nozaki, Daisuke Yashiro, and Kouhei Ohnishi, "Development of Two-link Manipulator Equipped with Biarticular Muscle Mechanism Using Flexible Actuator," *IEEJ Transactions on Industry Applications*, Vol. 132-D, No. 3, pp. 397–403, Mar. 2012. (in Japanese)

Journals (As a co-author)

[1] Satoshi Fukushima, Hiromu Sekiguchi, Yuki Saito, Wataru Iida, Takahiro Nozaki, and Kouhei Ohnishi, "Artificial Replacement of Human Sensation Using Haptic Transplant Technology," *IEEE Transactions on Industrial Electronics*, (accepted for publication).

[2] Takuya Matsunaga, Daisuke Tomizuka, Takahiro Nozaki, Yuki Saito, Kenji Ogawa, Kouhei Ohnishi, Norihito Wada, and Yuko Kitagawa, "Development of Miniature Haptic Forceps for Flexible Endoscope," *Journal of Japan Society of Computer Aided Surgery*, Vol. 19, No. 3, Vol. 19, No. 3, pp. 123-130, Jul. 2017. (in Japanese)

[3] Takahiro Nozaki, Takahiro Mozoguchi, Yuki Saito, Daisuke Yashiro, and Kouhei Ohnishi, "Recognition of Grasping Motion Based on Modal Space Haptic Information Using DP Pattern-Matching Algorithm," *IEEE Transactions on Industrial Informatics*, Vol. 9, No. 4, pp. 2043–2051, Nov. 2013.

[4] Koyo Yu, Yuki Saito, Yusuke Kasahara, Hiromasa Kawana, Shin Usuda, and Kouhei Ohnishi, "Bone Density Estimation Method for Robotic Drilling System," *IEEJ Transactions on Industry Applications*, Vol. 133-D, No. 3, pp. 328–334, Mar. 2013. (in Japanese)

[5] Takahiro Nozaki, Takahiro Mozoguchi, Yuki Saito, Tomohiro Nakano, and Kouhei Ohnishi, "Bilateral Control Method Based on Transformation Matrix Relating Motion Features and Tool Coordinates," *IEEJ Journal of Industry Applications*, Vol. 2, No. 1, pp. 67–73, Jan. 2013.

International Conference (As a first author)

[1] Yuki Saito, Takahiro Nozaki, Toshiyuki Murakami, and Kouhei Ohnishi, "Sensorless Position Estimation Method for Odd-numbered slots Brushed DC Motor," In *Proceedings of the IEEJ International Workshop on Sensing, Actuation, Motion Control*, Tokyo, Japan, Mar. 7th–8th, 2016.

[2] Yuki Saito, Uichiro Nishio, Takahiro Nozaki, and Kouhei Ohnishi, "Acceleration based Position and Force Control for Twist Drive," In *Proceedings of the 4th IEEE International Conference on Mechatronics*, Vicenza, Italy, Feb. 27th–Mar. 1st, 2013.

[3] Yuki Saito, Takahiro Nozaki, and Kouhei Ohnishi, "Model-based Compensation of Wire Elongation for Tendon-driven Rotary Actuator," In *Proceedings of the 12th IEEE International Workshop on Advanced Motion Control*, Sarajevo, Bosnia and Herzegovina, Mar. 25th–27th, 2012.

International Conference (As a co-author)

[1] Satoshi Fukushima, Hiromu Sekiguchi, Yuki Saito, Takahiro Nozaki, and Kouhei Ohnishi, "Online Compensation of Gravity and Friction for Haptics with Incremental Position Sensors," In *Proceedings of the 24th International Conference on Mechatronics and Machine Vision in Practice*, Auckland, New Zealand, Nov. 21st–23rd, 2017.

[2] Satoshi Fukushima, Hiromu Sekiguchi, Yuki Saito, Takahiro Nozaki, and Kouhei Ohnishi, "Haptic Telepresence System with Multi-Degrees of Freedom Exoskeleton and Humanoid Robot," In *Proceedings of the IEEJ International Workshop on Sensing, Actuation, Motion Control, and Optimization*, Nagaoka, Japan, Mar. 6th–8th, 2017.

[3] Simon Lemerle, Satoshi Fukushima, Yuki Saito, Takahiro Nozaki , and Kouhei Ohnishi, "Wearable Finger Exoskeleton using Flexible Actuator for Rehabilitation," In *Proceedings of the IEEE 2017 International Conference on Mechatronics*, Gippsland, Australia, Feb. 13th–15th, 2017.

[4] Takahiro Nozaki, Kazuki Tanida, Takahiro Mizoguchi, Tomohiro Nakano, Yuki Saito, and Kouhei Ohnishi, "Extraction and Realization of Human Actions," In *Proceedings of the 13th International Workshop on Advanced Motion Control*, Yokohama, Japan, Mar. 14th–16th, 2014.

[5] Tomoniro Nakano, Yuki Saito, Takahiro Nozaki, and Kouhei Ohnishi, "Variable Tension Control for Master-Slave Tendon-Driven Robot Hand," In *Proceedings of the 4th IEEE International Conference on Mechatronics*, Vicenza, Italy, Feb. 27th–Mar. 1st, 2013.

[6] Kasun Prasanga, Yuki Saito, Takahiro Nozaki, and Kouhei Ohnishi, "Achievement of real haptic sensation with tendon driven segregated jaws for laparoscopic forceps," In *Proceedings of the 6th International Conference on Information and Automation for Sustainability*, Beijing, China, Sep. 27th–29th, 2012.

Domestic Conference (As a first author)

[1] Yuki Saito, Uichiro Nishio, Takahiro Nozaki and Kouhei Ohnishi, "Realization of Acceleration based Control for Strings Transmission Twist Drive," In *Proceedings of the IEEJ Industry Applications Society Conference,*, Aug. 21st–23rd, 2012. (in Japanese)

[2] Yuki Saito, Takahiro Nozaki, Tomohiro Nakano, and Kouhei Ohnishi, "Analysis and Compensation of Wire Elongation for Tendon-driven Rotary Actuator Based on Four-element Viscoelastic model," In *Papers of the IEEJ Technical Meeting on Industrial Instrumentation and Control,*, Mar. 6th–7th, 2012. (in Japanese)

[3] Yuki Saito, Takahiro Nozaki, Kouhei Ohnishi, Yasuhide Morikawa, and Souji Ozawa, "Scaling Bilateral Control of Tendon-driven Rotary Actuator," In *Journal of Japan Society of Computer Aided Surgery,*, Nov. 22nd–24th, 2011. (in Japanese)

[4] Yuki Saito, and Kouhei Ohnishi, "A Novel Approach for Torque Sharing Problem of Two Link Manipulator Equipped with Bi-articular Muscle Mechanism," In *Proceedings of the IEEJ Industry Applications Society Conference,*, Sep. 6th–8th, 2011. (in Japanese)

[5] Yuki Saito, Wataru Motooka, Takahiro Nozaki, and Kouhei Ohnishi, "Development of Two-link Manipulator Equipped with Biarticular Muscle Mechanism Using Flexible Actuator," In *Papers of the IEEJ Technical Meeting on Industrial Instrumentation and Control,*, Mar. 8th–9th, 2011. (in Japanese)